Gondwana Research 72 (2019) 97–119

Contents lists available at ScienceDirect

Gondwana Research

journal homepage: www.elsevier.com/locate/gr

Generation of high-Mg diorites and associated iron mineralization within an intracontinental setting: Insights from ore-barren and ore-bearing intrusions in the eastern North China Craton

Ting-Guang Lan [a,b,*], Rui-Zhong Hu [a,b], Ying-Hua Chen [a,b], Hong Wang [a,b], Yan-Wen Tang [a], Liang Liu [a]

[a] State Key Laboratory of Ore Deposit Geochemistry, Institute of Geochemistry, Chinese Academy of Sciences, Guiyang 550081, China
[b] College of Earth Sciences, University of Chinese Academy of Sciences, Beijing 100049, China

ARTICLE INFO

Article history:
Received 3 September 2018
Received in revised form 22 February 2019
Accepted 1 March 2019
Available online 4 April 2019

Handling Editor: Z.M. Zhang

Keywords:
High-Mg diorite
Fe skarn deposit
Crustal contamination
Mantle metasomatism
North China Craton

ABSTRACT

High-Mg andesitic rocks (HMAs) are commonly generated through slab-mantle interactions in arc settings. In this study, however, we report the high-Mg diorites in the Zibo and Laiwu areas of the eastern North China Craton (NCC), which were particularly produced during lithospheric thinning within an intracontinental setting. Some of the rocks generated large-scale Fe skarn deposits (e.g., the Zibo quartz monzonite and the Laiwu Kuangshan monzonite), whereas the others are ore-barren (e.g., the Zibo gabbroic diorite and the Laiwu Jinniushan and Jiaoyu monzodiorites), providing an excellent case to reveal how the non-arc HMAs were formed and the crucial factors controlling the Fe mineralization. All the rocks are characterized by high Mg# values (51–84) at andesitic compositions (52.5–65.0 wt%) and show arc-like geochemistry (e.g., enriched in LREEs and LILEs and depleted in HREEs and HFSEs), of which the strongly mineralized intrusions are more felsic with higher Mg# values (69–84) and stronger fractionation between LREEs and HREEs. Zircon U-Pb dating indicates that these rocks were emplaced at the early Cretaceous (130–132 Ma), coeval with the peak thinning of the lithosphere in the eastern NCC. All the rocks have transitional Sr-Nd-Pb isotopic compositions ($0.704726 < (^{87}Sr/^{86}Sr)_i < 0.707507$, $-16.0 < \varepsilon_{Nd}(t) < -5.4$, $16.334 < (^{206}Pb/^{204}Pb)_i < 17.629$, $15.205 < (^{207}Pb/^{204}Pb)_i < 15.447$, $36.306 < (^{208}Pb/^{204}Pb)_i < 37.754$) between the local lithospheric mantle and the ancient crust. Combined with their high Mg# and arc-like geochemistry, they were most likely derived from an anciently metasomatized and recently hydrated sub-continental lithospheric mantle (SCLM) with various crustal contamination. Magma mixing modelling suggests that in the Zibo area little crustal materials were involved into the gabbroic diorite, but ~20% middle-upper crustal materials were assimilated into the monzodiorite and quartz monzonite during magma ascent. In the Laiwu area, lower crustal materials (at least ~30%) were significantly involved into the Jinniushan, Jiaoyu and Kuangshan intrusions through magma mixing at the base of the lower crust. Sedimentary rocks (mainly carbonates interbedded with coal-bearing shales, sandstones and evaporitic rocks) were particularly assimilated into the strongly mineralized intrusions in both the Zibo and Laiwu areas. Such assimilation probably contributed to promote fluid exsolution and metal extraction from the melts, since the strongly mineralized intrusions have the lowest H_2O contents (2.4–3.2 wt% H_2O), the highest Mg# values and the lowest oxygen fugacities ($2.5 < \Delta FMQ < 3.1$). It is thus considered that the assimilation of sedimentary rocks is crucial for generating ore-forming fluids. P-T calculations indicate that all the high-Mg diorites were emplaced shallowly (mainly $T < 760$ °C and $P < 140$ MPa). In combination with the co-development of bimodal volcanics, metamorphic core complexes and rift basins in the eastern NCC during the early Cretaceous, extreme lithospheric extension should have occurred in the study region. Such intracontinental extension was likely caused by the asthenospheric upwelling induced by the stagnant Paleo-Pacific Plate in the transition zone beneath the eastern Asian continent. The geodynamic regime is different from those of the typical arc settings.

1. Introduction

High-Mg andesitic rocks (HMAs) are characterized by high Mg# values (>50) and/or MgO contents (>6 wt%) at andesitic compositions ($SiO_2 > 54$ wt%) (Kelemen et al., 2003). Although small volumes in modern earth magmatism, the HMAs are of great interest because their

* Corresponding author at: Institute of Geochemistry, Chinese Academy of Sciences, No.99 Linchengxi Road, Guiyang, Guizhou Province 550081, China.
E-mail address: lantingguang@126.com (T.-G. Lan).

https://doi.org/10.1016/j.gr.2019.03.008
1342-937X/

compositions approximate average continental crust and thus can provide insights into the mode of continental growth (Kelemen, 1995; Rudnick, 1995; Tatsumi, 2008). They have been commonly considered to be generated through various slab-mantle interactions in arc settings, such as slab melts (±sediment components) reacting with mantle peridotite (e.g., Yogodzinski et al., 1995; Tatsumi, 2001; König et al., 2007; Wang et al., 2011), or partial melting of mantle peridotite previously metasomatized by slab melts/fluids (e.g., Cole et al., 2000; Calmus et al., 2003; Martin et al., 2005; Manya et al., 2007). Due to the involvement of slab materials, the HMAs have good potentials to produce economic deposits, such as porphyry or skarn Cu-Au deposits (e.g., Mueller, 2007; S.A. Liu et al., 2010; Lin and Beakhouse, 2013; Yang et al., 2015; Deng et al., 2017). It has been well understood that in arc settings the oceanic slabs can effectively transport water, sulfur, metals and oxidative seafloor materials into the mantle wedge, which facilitate Cu-Au mineralizations (Mungall, 2002; Richards, 2011; Wilkinson, 2013). In recent years, however, more and more evidence shows that the HMAs can not only be produced in arc settings, but also in non-arc settings, such as collisional (e.g., Lin and Beakhouse, 2013; Yang et al., 2015), post-collisional (e.g., Jahn et al., 1999; Sajona et al., 2000; Karsli et al., 2010) and intracontinental extensional settings (e.g., Gao et al., 2008; Pirajno et al., 2009; Qian and Hermann, 2010). In addition, iron and Cu-Au mineralizations associated with the non-arc HMAs have also been reported (e.g., Lin and Beakhouse, 2013; Jin et al., 2015; Yang et al., 2015; Zhang et al., 2014). This begs the questions: How do the non-arc HMAs originate? What are the crucial factors controlling the mineralization?

Early Cretaceous high-Mg diorites are widely distributed in the Handan-Xingtai area of central North China Craton (NCC) and the Luxi Block of eastern NCC (Fig. 1). These rocks typically show high Mg# and arc-like geochemistry similar to those generated in arc settings, but they have been consistently considered to occur during lithospheric thinning within an intracontinental setting (Gao et al., 2008; Qian and Hermann, 2010). Some of the high-Mg diorites were mineralized, producing large-scale Fe and minor Cu-Au skarn deposits (Kong et al., 2006; Zhang et al., 2014; Jin et al., 2015; Sun et al., 2015; Zhang et al., 2015). They thus provide an excellent case to study how the HMAs as well as the associated mineralizations were generated in non-arc setting. The genesis of these rocks remains controversial, with at least four representative models being proposed: (1) partial melts of delaminated continental lower crust interacting with mantle peridotite (e.g., Gao et al., 2008; Xu et al., 2008), (2) partial melts of enriched lithospheric mantle previously metasomatized by subducted or delaminated continental crust (e.g., Huang et al., 2012; D.B. Yang et al., 2012; Q.L. Yang et al., 2012), (3) magma mixing between siliceous crustal melts and basaltic magmas from metasomatized mantle

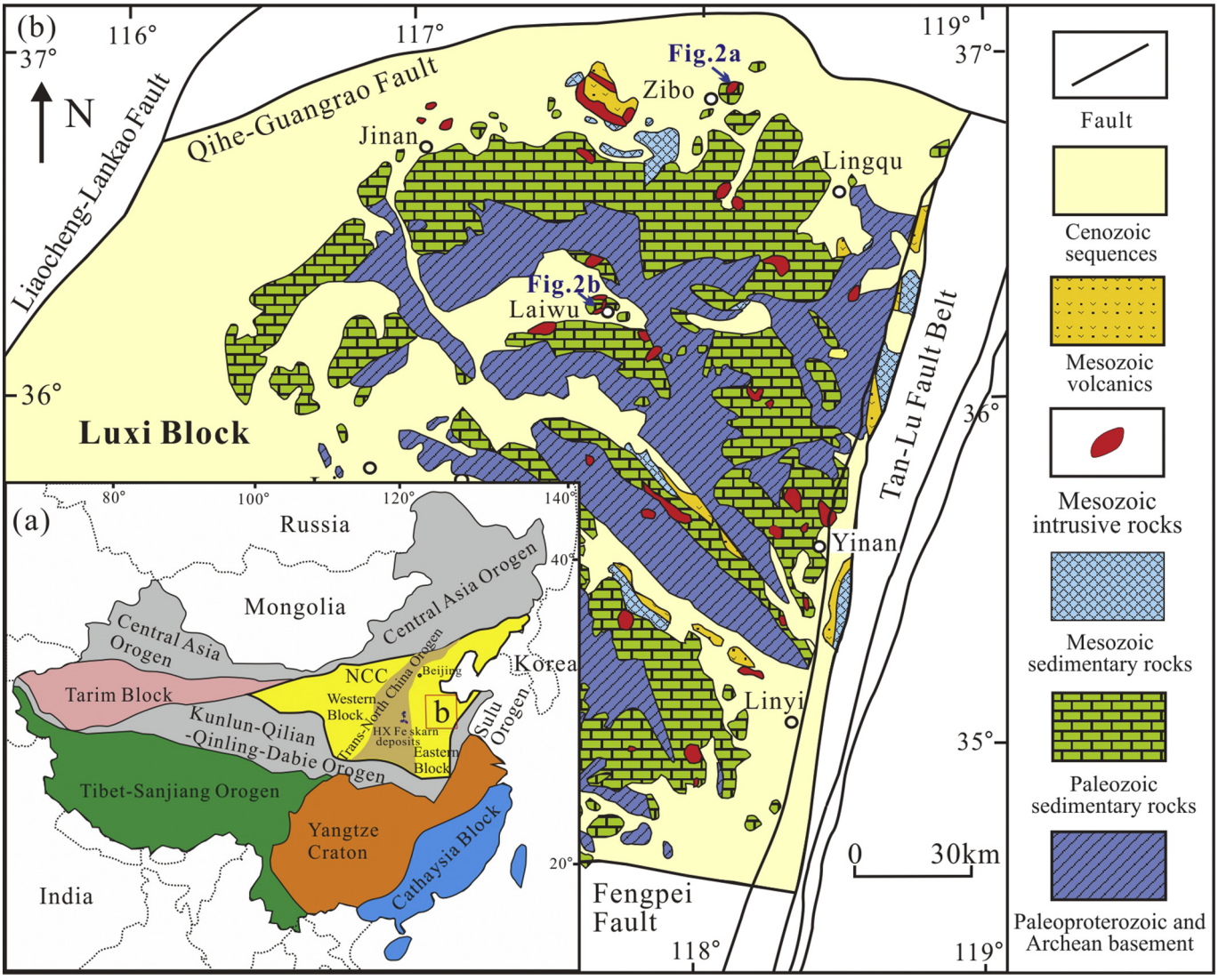

Fig. 1. Tectonic subdivision of China (a) and geological map of the Luxi Block (b). (a) is modified after Mao et al. (2011), and (b) is modified after Zhang et al. (2007). The Fe skarn deposits associated with high-Mg diorites in the HX (Handan-Xingtai) area are also shown in (a) (modified after Jin et al., 2015).

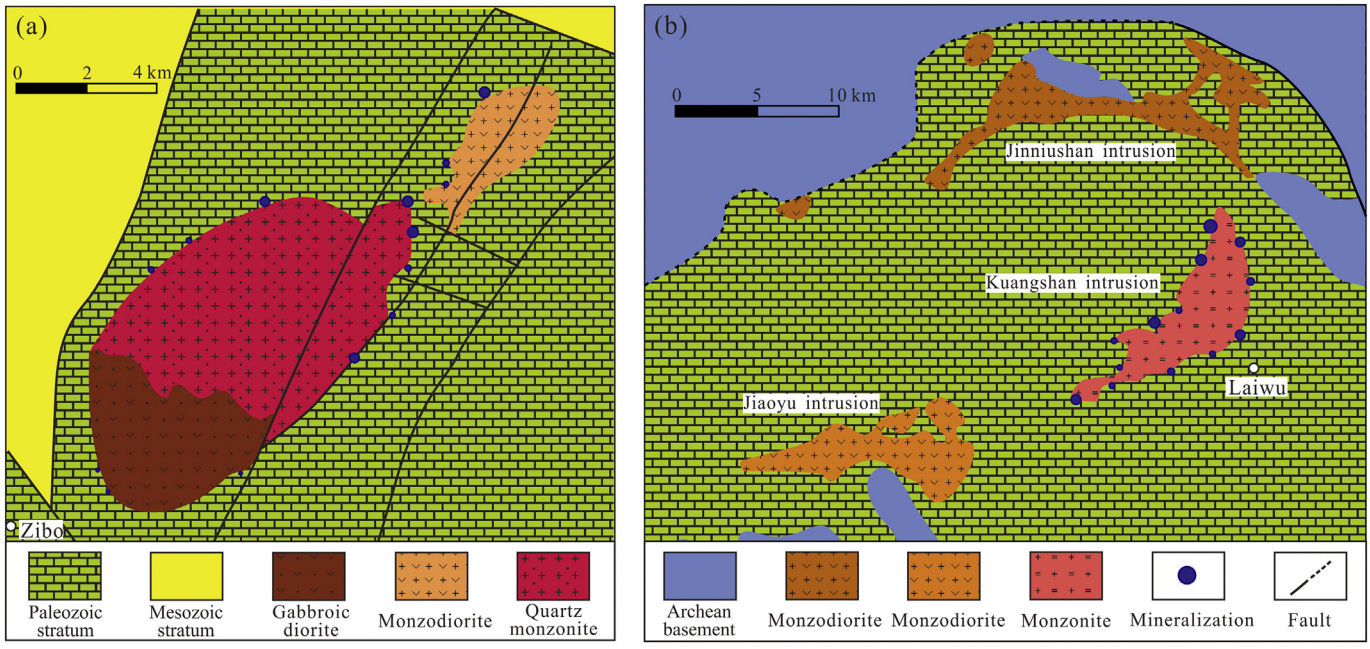

Fig. 2. Geological maps of the Zibo (a) and Laiwu (b) high-Mg diorites and the distribution of associated iron deposits. (a) and (b) are modified after Kong et al. (2006) and Zong et al. (2010), respectively.

(e.g., Chen et al., 2013), and (4) assimilation of previously emplaced mantle peridotite by crust-derived monzodioritic magmas at crustal depth (e.g., Qian and Hermann, 2010). The metallogeny of these high-Mg diorites also attracted many attentions in recent years (e.g., Zong et al., 2010, 2011, 2012; Zhang et al., 2014; Jin et al., 2015; Sun et al., 2015; Zhang et al., 2015; Duan and Li, 2017), but most of the studies were limited to the ore deposits while how the magmas contributed to form the ore deposits was less concerned, leaving the magma-mineralization processes poorly constrained. In this contribution, we select the representative ore-barren and ore-bearing high-Mg diorites in the Zibo and Laiwu areas of the Luxi Block to carry out detailed analyses on zircon geochronology and geochemistry, in-situ mineral geochemistry (silicates and Fe-Ti oxides) and whole-rock geochemistry (major and trace elements and Sr-Nd-Pb isotopes), with the aim to (1) constrain the sources as well as the physicochemical conditions (e.g., temperature, pressure, H_2O content and oxidation state) of the high-Mg diorites, (2) contrast the ore-barren and ore-bearing intrusions and thus reveal the crucial factors controlling the Fe mineralization and (3) discuss the metallogeny and geodynamic regime of the non-arc high-Mg diorites.

2. Geological background

2.1. Regional geology

The North China Craton (NCC) is the largest and oldest craton in China (~1,500,000 km^2 in size with 2.5–3.8 Ga cores) (Fig. 1a), which is constituted mainly by a basement of Archean to Paleoproterozoic tonalitic-trondhjemitic-granodioritic (TTG) gneisses and greenschist to granulite facies volcano-sedimentary rocks and a cover of Mesoproterozoic to Neoproterozoic volcano-sedimentary rocks, Cambrian to Ordovician epicontinental carbonates, Carboniferous to Permian alternating marine and terrestrial sequences, and Mesozoic-Cenozoic basin sediments (Lu et al., 2008; Yang et al., 2017). It became a craton by amalgamation among several Archean micro-continental blocks before the Mesoproterozoic (Zhai and Santosh, 2011; Zhao et al., 2012). After cratonization, the NCC remained largely stable until the Mesozoic, prior to the remarkable thinning of the lithosphere (>120 km loss of the Archean lithosphere, Fan et al., 2000) beneath its central-eastern domains (referred to craton destruction, Zhu et al., 2012). Large-scale mafic to felsic magmatic activities as well as various mineralization types were induced by the lithospheric thinning (Li and Santosh, 2014; Wu et al., 2005). Multiple subduction and collisional events surrounding the NCC, such as the southward subduction of the Paleo-Asian Oceanic Plate below the northern margin of the NCC during the Ordovician and Permo-Triassic (Xiao et al., 2003), the northward continental collision between the South China Block (SCB) and the southern NCC during the Triassic (Li et al., 1993; Meng and Zhang, 1999) and the westward subduction of the Paleo-Pacific Plate underneath the eastern Asian continent during the Mesozoic, probably contributed to the craton destruction, of which the last one has been considered to play the dominant role (Windley et al., 2010; Zhu et al., 2012).

The Luxi Block is located at the eastern part of the NCC and is bounded by the Tan-Lu fault to the east, the Liaocheng-Lankao fault to the west, the Qihe-Guangrao fault to the north, and the Fengpei fault to the south (Fig. 1b). The Tan-Lu fault extends deeply into the mantle, which not only acted as a conduit for asthenospheric upwelling (Chen et al., 2006), but also controlled the emplacement of the widespread Mesozoic igneous rocks in the study region (Qiu et al., 2000; Ren et al., 2002). The igneous rocks include intrusive rocks such as gabbros, high-Mg diorites, high-K calc-alkaline to alkaline rocks, granites, mafic dykes and carbonatites and volcanic rocks varying from basalts to rhyolites. The high-Mg diorites, which are represented by the Jinling intrusive complex in the Zibo area (Jin et al., 2015), the Kuangshan, Jinniushan, Jiaoyu and Tietonggou intrusions in the Laiwu area (Zong et al., 2010; Duan and Li, 2017), the Tiezhai intrusion in the Linqu area and the Tongjing intrusion in the Yinan area (Zhang et al., 2011), were prone to produce Fe and Cu-Au skarn mineralizations. The mineralizations commonly occur in the contact zones between the high-Mg diorites and the Paleozoic carbonate rocks (Zong et al., 2010; Jin et al., 2015; Duan and Li, 2017). The strata in the Luxi Block are generally consistent with those of the NCC, but were deformed into a sandwiched structure between the Precambrian basement and the Phanerozoic cover (Fig. 1b). Notably, the Mesozoic lithospheric mantle beneath the Luxi Block varied from EM1 to EM2 from the northwest to the southeast, which has been commonly considered to be resulted from the metasomatism by the subducted SCB continental crust beneath the southeastern NCC (e.g., Xu et al., 2004b; Huang et al., 2012; D.B. Yang et al., 2012; Q.L. Yang et al., 2012).

2.2. The Zibo high-Mg diorites and related Fe deposits

Jinling intrusive complex is the dominant high-Mg pluton in the Zibo area, which is located at the northeast of the Zibo city with a SW-NE trend (Fig. 2a). It covers an area of ~70 km^2 and consists of three major lithologies, including gabbroic diorite in the southwest, monzodiorite in the northeast, and quartz monzonite in the middle. These rocks show an observed intrusive sequence from the gabbroic diorite to the monzodiorite and then to the quartz monzonite (Kong et al., 2006). The gabbroic diorite is moderate-grained and composed mainly of plagioclase (~45 vol%), amphibole (30–35 vol%) and alkaline feldspar (~10 vol%) with minor pyroxene (5–10 vol%) and biotite (~5 vol%) and accessory magnetite, titanite, zircon and apatite (Fig. 3a). The monzodiorite is fine-grained and composed mainly of plagioclase (~65 vol%), biotite (15–20 vol%) and alkaline feldspar (~15 vol%) without amphibole (Fig. 3b). Pyroxene and quartz sporadically occur. The accessory minerals are magnetite, ilmenite, zircon and apatite. The quartz monzonite is also fine-grained and consists mainly of plagioclase (60–65 vol%), alkaline feldspar (15–20 vol%) and amphibole (~15 vol%) with minor quartz (~5 vol %) and accessory magnetite-titanomagnetite, zircon and apatite (Fig. 3c).

More than ten Fe skarn deposits have been found in the contact zones between the Jinling intrusive complex and the Paleozoic carbonate rocks (Fig. 2a). The total iron reserves reported so far are about 200 million tons, with an average Fe grade of ~52% (Ma et al., 2004; Jin et al., 2015). Copper and Co accompany the Fe mineralization, with metal grades of 0.1–0.2% and 0.01–0.02%, respectively. It is noteworthy that different rocks show contrasted metallogenic potentials. The gabbroic diorite has the weakest metallogenic potential and just gave rise to <0.2 million tons of iron ores, whereas the monzodiorite has the moderate metallogenic potential and accounts for about 56 million tons of iron ores. The quartz monzonite shows the strongest metallogenic potential, producing >100 million tons of iron ores. In order to facilitate the discussion below, the above rocks are regarded as ore-barren, moderately and strongly mineralized, respectively.

2.3. The Laiwu high-Mg diorites and related Fe deposits

The Laiwu high-Mg diorites are located <100 km to the south of the Zibo high-Mg diorites. They mainly include the Jinniushan, Jiaoyu and Kuangshan intrusions, which are situated at the northwest to southwest of the Laiwu city and cover a total area of about 100 km^2 (Fig. 2b). The Jinniushan intrusion is a fine-grained monzodiorite and composed mainly of plagioclase (~50 vol%), amphibole (~40 vol%) and alkaline feldspar (~10 vol%) with accessory magnetite, zircon and apatite (Fig. 3d). The Jiaoyu intrusion is also a fine-grained monzodiorite, but contains biotite absent in the Jinniushan intrusion. It consists mainly of plagioclase (45–50 vol%), amphibole (~35 vol%), alkaline feldspar (10–15 vol%) and biotite (~5 vol%) with minor pyroxene (Fig. 3e). The accessory minerals are magnetite, ilmenite, zircon and apatite. The Kuangshan intrusion is a fine-grained monzonite, which is composed mainly of plagioclase (65–70 vol%), amphibole (~20 vol%) and alkaline feldspar (5–10 vol%) with minor quartz (<5 vol%) and accessory magnetite-titanomagnetite, rutile, zircon and apatite (Fig. 3f).

More than twenty Fe skarn deposits have been found around these rocks (Fig. 2b), which account for about 505 million tons of iron reserves with the common Fe grades of 45–50%. The majority (~98.8%) of the above reserves is associated with the Kuangshan intrusion, whereas just about 0.9% and 0.3% are related to the Jinniushan and Jiaoyu intrusions (Zong et al., 2011). Considering the contrasted metallogenic potentials among them, the Jinniushan and Jiaoyu intrusions are regarded as ore-barren. The mineralization also mainly occurs in the contact zones between the intrusions and the Paleozoic carbonate rocks (Duan and Li, 2017), similar to that in the Zibo area. Copper and Co accompany the Fe mineralization, showing metal grades of 0.03–0.56% (averaging at 0.09%) and 0.01–0.03% (averaging at 0.02%) (Zong et al., 2012), respectively.

3. Analytical methods

Scanning electron microscope (SEM) and electron probe microanalyzer (EPMA) were used to conduct mineral imaging and major element analyses. Laser ablation inductively coupled plasma mass spectrometry (LA-ICP-MS) was used for zircon U-Pb dating and trace element analyses in zircon and Fe-oxides (mainly magnetite). X-ray fluorescence spectroscopy (XRF) and ICP-MS were used for whole-rock major and trace element analyses, respectively. Multi-collector ICP-MS (MC-ICP-MS) was used to analyze the whole-rock Sr-Nd-Pb isotopic compositions.

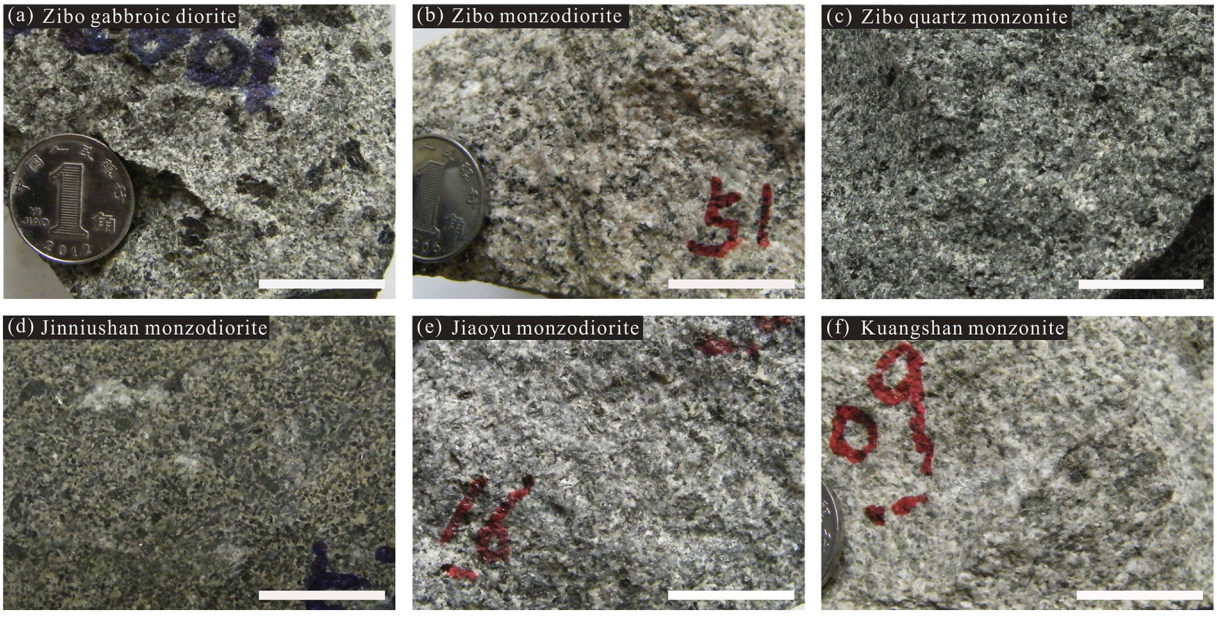

Fig. 3. Photographs of representative rock samples from the Zibo (a, b and c) and Laiwu (d, e and f) high-Mg diorites. The scale bar is 2 cm in each picture.

3.1. SEM and EPMA analyses

In order to identify internal textures and choose potential target sites for in-situ U-Pb dating and trace element analyses, cathodoluminescence (CL) and back-scattered electron (BSE) imaging of minerals were obtained using a JSM-7800F SEM at the State Key Laboratory of Ore Deposit Geochemistry (SKLODG), Institute of Geochemistry, Chinese Academy of Sciences (IGCAS), Guiyang, China. The working conditions were 10 kV accelerating voltage and 10 nA beam current for CL and 20 kV accelerating voltage and 10 nA beam current for BSE, respectively.

The major elements in silicate minerals were determined using an EPMA-1600 EPMA at the SKLODG, whereas Fe-oxides were measured using a JXA-8230 EPMA at the Shandong Institute of Geological Sciences, Jinan, China. The working conditions were 25 kV accelerating voltage and 10 nA beam current for the silicate minerals while 15 kV accelerating voltage and 20 nA beam current were used for the Fe-Ti oxides.

3.2. LA-ICP-MS analyses

The U-Pb dating and trace element analyses of zircon were conducted by LA-ICP-MS at the SKLODG. Laser sampling was performed using a GeoLasPro 193 nm ArF excimer laser. An Agilent 7900 ICP-MS was used to acquire ion-signal intensities. Each analyses incorporated a background acquisition of approximately 20 s (gas blank) followed by 50 s data acquisition from the sample. Helium was used as the carrier gas. Argon was used as the makeup gas and mixed with the carrier gas via a T-connector before entering the ICP. Laser spot size of 32 μm and repetition of 6 Hz were used during the analyses. Zircon 91500 was used as the external standard for U-Th-Pb calibrations, and was analyzed twice every 5 analyses. NIST SRM610 was used as the external standard for trace element calibrations, and was analyzed twice every 10 analyses. Combined with using Zr as internal standard, this approach has the advantage to accurately measure the trace element concentrations in zircon (Y.S. Liu et al., 2010). Off-line selection and integration of background and analyte signals, time-drift correction, and quantitative calibrations were performed by *ICPMSDataCal* (Liu et al., 2008). Concordia diagrams and weighted mean calculations were made using *ISOPLOT* software (Ludwig, 2003). The preferred values of element concentrations for the NIST SRM610 are from the GeoReM database. Detailed data calibrations refer to Y.S. Liu et al. (2008, 2010).

The determination of trace element concentrations in magnetite was also conducted at the SKLODG using an Agilent 7700x ICP-MS equipped with a GeoLasPro 193 nm ArF excimer laser. Laser repetition of 4 Hz, energy density of 6 J/cm^2 and spot size of 32 μm were used during the analyses. Each analyses incorporated a background acquisition of approximately 20 s followed by 50 s data acquisition from the sample. Referring to the method of Nadoll and Koenig (2011), GSE-1G was used as the external standard while the iron content obtained from the EPMA was used as the internal standard for the trace element concentration calculations. GOR-128g and BCR-2G were used to monitor the precision and accuracy of the calibration, the results of which are generally within 10% analytical error of the working values. All the reference materials were analyzed twice every 10 analyses. Off-line selection and quantitative calibrations were also performed by the *ICPMSDataCal* software.

3.3. Whole-rock major and trace element analyses

Whole-rock major and trace element analyses were conducted at the ALS Laboratory Group in Guangzhou, China. For major element analyses, 200 mesh whole-rock powders were admixed with $Li_2B_4O_7$ and fused into glass discs at temperature higher than 1025 °C. The discs were then analyzed by a Philips PW2404 XRF. Basaltic to granitic rock standards (NCSDC73303, SARM-2, SARM-3, and SARM-4) were analyzed to monitor the analytical quality, the results of which indicate the accuracy of better than 2%. Ferrous iron (Fe^{2+}) was analyzed independently using the dichromate method.

For trace element analyses, whole-rock powders were dissolved in distilled HF + HNO_3 + $HClO_4$ mixture, dried, and then digested with HCl. The final solutions were analyzed using an Agilent 7700x ICP-MS. The analytical uncertainties are within 5% for most elements, as indicated by the analyses of standard materials of GBM908-10, MRGeo08, OREAS460 and SY-4.

3.4. Whole-rock Sr-Nd-Pb isotopic analyses

The whole-rock Sr, Nd and Pb isotopic analyses were performed at the Radiogenic Isotope Facility, University of Queensland, Australia. About 70 mg rock powders were dissolved with HF-HNO_3 mixture in Teflon bombs at 180 °C in an oven for 3 days, and dried down on a hot plate at 80 °C. After converting any fluoride to nitrate, the dried residues were digested with 3 ml 2 N HNO_3 and passed through column chemistry to separate Sr, Nd and Pb from matrix using the methods described in Wei et al. (2014). Typical procedural blanks are about 65, 60 and 50 pg for Sr, Nd and Pb, respectively.

All the Sr, Nd and Pb isotopic compositions were analyzed using a Nu Plasma MC-ICP-MS. The Sr and Nd isotopic ratios were corrected for mass fractionation by normalizing to $^{86}Sr/^{88}Sr = 0.1194$ and $^{146}Nd/^{144}Nd = 0.7219$, respectively. Standards were measured to monitor the detector efficiency drift of the instrument and the accuracy of the analytical procedures. The repeated analyses of Sr standard NBS-987 during our samples yielded an average $^{87}Sr/^{86}Sr$ of 0.710336 ± 22 (2σ). The deviation of this mean value from the laboratory's previously obtained long-term average value of 0.710249 ± 28 (2σ, by a VG Sector 54 TIMS, Wei et al., 2014) was used to correct for all samples. The Nd standard of Ames Nd Metal yielded an average $^{143}Nd/^{144}Nd$ of 0.511965 ± 8 (2σ), very close to the accepted value (0.511966 ± 16, Wei et al., 2014). Lead separated by column chemistry was doped with 4 ppb Tl with a $^{205}Tl/^{203}Tl$ ratio of 0.23875 used for mass fractionation correction. The repeated analyses of Pb standard NBS-981 yielded average ratios of $^{206}Pb/^{204}Pb = 16.946 \pm 0.002$, $^{207}Pb/^{204}Pb = 15.496 \pm 0.002$ and $^{208}Pb/^{204}Pb = 36.704 \pm 0.003$. The Pb isotopic data were corrected by the recommended NBS-981 values of $^{206}Pb/^{204}Pb = 16.941$, $^{207}Pb/^{204}Pb = 15.494$, $^{208}Pb/^{204}Pb = 36.718$ (Collerson et al., 2002). The USGS reference materials BCR-2 and BHVO-2 were also analyzed with our samples, the results of which are consistent with the recommended values (GeoREM: http://georem.mpch-mainz.gwdg.de/) within errors.

4. Analytical results

4.1. Zircon U-Pb dating

Fresh samples (unaltered and unweathered) were selected for zircon U-Pb dating. The results are shown in Fig. 4 and summarized in Supplementary Table S1.

4.1.1. The Zibo high-Mg diorites

The zircons in the gabbroic diorite (13ZB01) are euhedral to subhedral with the sizes of 100–200 μm. Patch zoning rather than oscillatory zoning is featured in these zircons (Fig. 4a), although oscillatory zoning is also ubiquitous at the rims. The ages in different zones are consistent. Twenty analyses conducted on 20 zircon grains plot on the concordia, generating a concordia intercept age of 131.8 ± 1.0 Ma (MSWD = 0.1) and a weighted mean $^{206}Pb/^{238}U$ age of 131.6 ± 0.8 Ma (MSWD = 0.2) (Fig. 4a).

The zircons from the monzodiorite (16ZB01) are granular and euhedral to subhedral with sizes of 100–150 μm. They are grey in CL images and show patch to sector zonings (Fig. 4b). Twenty-one analyses conducted on 21 zircon grains are consistent and concordant,

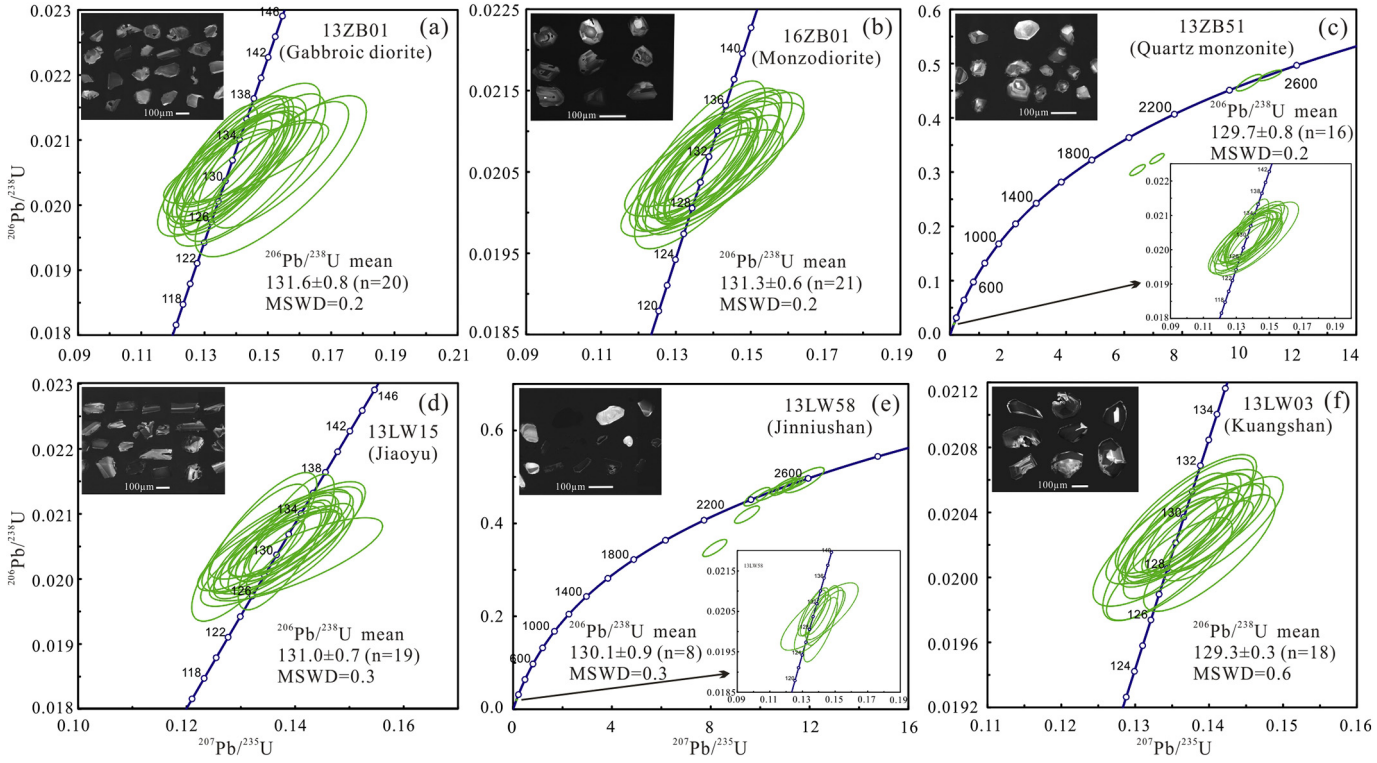

Fig. 4. Concordia plots for U-Pb isotopic data and CL images of zircons from the Zibo (a, b and c) and Laiwu (d, e and f) high-Mg diorites.

generating a concordia intercept age of 131.4 ± 1.9 Ma (MSWD = 0.1) and a weighted mean $^{206}Pb/^{238}U$ age of 131.3 ± 0.6 Ma (MSWD = 0.2) (Fig. 4b).

Most of the zircons from the quartz monzonite (13ZB51) are grey in CL images, but a few are comparatively white (Fig. 4c). Sixteen analyses conducted on 16 grey zircon grains are consistent and concordant, yielding a concordia intercept age of 130.1 ± 1.5 Ma (MSWD = 0.1) and a weighted mean $^{206}Pb/^{238}U$ age of 129.7 ± 0.8 Ma (MSWD = 0.2) (Fig. 4c). Four analyses conducted on grey-white zircons give much older ages, showing the $^{207}Pb/^{206}Pb$ ages of 2389–2524 Ma. The old zircons are not so concordant and are interpreted to be captured zircons.

From the ore-barren gabbroic diorite to the strongly mineralized quartz monzonite, the intrusive age gradually becomes younger, consistent with their field relationships. In addition, captured zircons have only been found in the strongly mineralized quartz monzonite.

4.1.2. The Laiwu high-Mg diorites

Zircons from the Jiaoyu monzodiorite (13LW15) are subhedral to anhedral with 100–200 μm in size. They are grey in CL images and do not show significant zoning (Fig. 4d). Nineteen analyses conducted on 19 zircon grains construct a concordia intercept age of 131.0 ± 0.7 Ma (MSWD = 0.3) and give a weighted mean $^{206}Pb/^{238}U$ age of 131.0 ± 0.6 Ma (MSWD = 0.3) (Fig. 4d).

Zircons in the Jinniushan monzodiorite (13LW58) are rare and show columnar to granular shapes. The columnar zircons are commonly dark in CL images while the granular zircons are grey to white with rounded shapes. Eight analyses conducted on 8 dark zircon grains construct a concordia intercept age of 130.7 ± 1.6 Ma (MSWD = 0.2) and a weighted mean $^{206}Pb/^{238}U$ age of 130.1 ± 0.9 Ma (MSWD = 0.3) (Fig. 4e). Ten grey to white zircons give much older ages, showing the $^{207}Pb/^{206}Pb$ ages of 2433–2585 Ma.

The zircons in the Kuangshan monzonite (13LW03) are commonly subhedral to anhedral with sizes of 100–300 μm. They are generally grey to dark in CL images and show patch zoning instead of oscillatory zoning (Fig. 4f). Eighteen analyses conducted on 18 zircon grains generate a concordia intercept age of 129.5 ± 0.6 Ma (MSWD = 0.5) and a weighted mean $^{206}Pb/^{238}U$ age of 129.3 ± 0.3 Ma (MSWD = 0.6) (Fig. 4f).

The Laiwu intrusions show similar intrusive ages to those of the Zibo rocks, and the strongly mineralized intrusion is also characterized by the youngest age, but the captured zircons occur in the more mafic rock.

4.2. Geochemistry of zircon

Rare earth elements (REEs) and Ti are the meaningful elements in zircon, which can be used to estimate the compositions (e.g., Heaman et al., 1990; Belousova et al., 2002; Hanchar and van Westrenen, 2007), the oxidation states (e.g., Ballard et al., 2002; Trail et al., 2012; Burnham and Berry, 2014; Smythe and Brenan, 2016) and the crystallization temperatures (e.g., Watson and Harrison, 2005; Watson et al., 2006; Ferry and Watson, 2007) of the host magmas. All the zircons from the high-Mg diorites have similar REE distribution patterns, showing depletion in LREEs and enrichment in HREEs with notable positive Ce and negative Eu anomalies (Fig. 5 and Supplementary Table S2). However, the REEs in the Laiwu zircons show much higher concentrations and larger variations than those in the Zibo zircons. The zircons from the Laiwu Jinniushan intrusion have the highest LREE concentrations. In addition, the Th and U concentrations as well as the Th/U and Zr/Hf ratios are higher in the Laiwu zircons than in the Zibo zircons.

The Ti contents of zircons in the Zibo high-Mg diorites increase slightly from the ore-barren gabbroic diorite (11.2–21.8 ppm, averaging at 15.5 ppm) to the moderately mineralized monzodiorite (12.8–29.7 ppm, averaging at 21.0 ppm), but decrease obviously to the strongly mineralized quartz monzonite (6.8–14.8 ppm, averaging at 10.3 ppm) (Supplementary Table S2). For the Laiwu high-Mg diorites, the zircons in the earliest ore-barren Jiaoyu monzodiorite have the lowest Ti contents (3.0–10.9 ppm, averaging at 5.6 ppm), while those in the strongly mineralized Kuangshan monzonite have higher (6.6–12.1 ppm, averaging at 9.5 ppm). The Jinniushan monzodiorite shows the largest variation of Ti contents in zircons (4.0 to 19.2 ppm, average at 10.1 ppm).

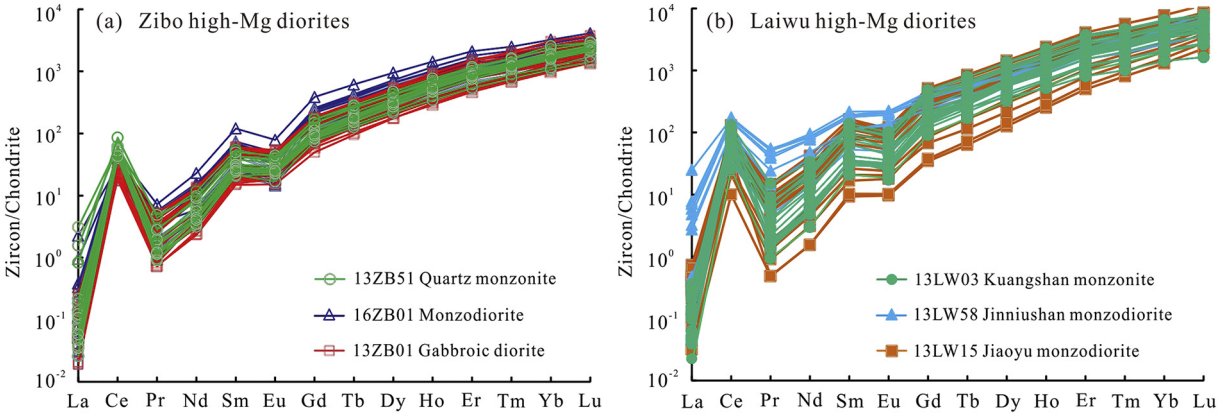

Fig. 5. Chondrite-normalized REE distribution patterns for zircons from the Zibo (a) and Laiwu (b) high-Mg diorites.

4.3. Geochemistry of silicate minerals

Amphibole, feldspar, pyroxene and biotite are the major silicate minerals in the high-Mg diorites, all of which were measured by EPMA for major element contents (Table 2 and Supplementary Table S3). The feldspar is mainly oligoclase to andesine (An_{18-51}) in all the high-Mg diorites. Minor albite (An_{1-10}) and orthoclase (Or_{77-99}) occur in the ore-barren intrusions, whereas they are absent in the strongly mineralized intrusions. The pyroxene is augite and diopside respectively in the Zibo and Laiwu intrusions, which shows lower FeO but higher CaO contents in the latter. Biotite has lower TiO_2 and K_2O but higher SiO_2 contents in the Laiwu intrusions than in the Zibo intrusions.

The nomenclature of amphibole is based on the International Mineralogical Association (IMA) classification (Hawthorne et al., 2012) and calculated using an excel spreadsheet from Locock (2014). Magnesio-ferri-hornblende, magnesio-hornblende, pargasite and actinolite are the common amphiboles in the high-Mg diorites (Table 2). For the Zibo intrusions, the magnesio-ferri-hornblende is dominant in the ore-barren gabbro diorite, while the actinolite is dominant in the strongly mineralized quartz monzonite. The former has higher MgO but lower FeO contents than those in the latter. For the Laiwu intrusions, the magnesio-ferri-hornblende is dominant in all the rocks, but it has much higher MgO and lower FeO contents in the strongly mineralized Kuangshan monzonite. The amphiboles in the Jinniushan and Jiaoyu intrusions show similar compositions except the Al_2O_3 contents which are significantly higher in the Jinniushan intrusion.

4.4. Geochemistry of magnetite

Magnetite, titanomagnetite and ilmenite are the common Fe-oxides in the Zibo and Laiwu high-Mg diorites. The FeO contents of magnetite decrease with increasing TiO_2 from the ore-barren to the strongly mineralized intrusions. In addition, for the strongly mineralized intrusions, the TiO_2 contents of magnetite are higher in the Zibo quartz monzonite (>20 wt%) than those in the Laiwu Kuangshan monzonite (3–6 wt%) (Fig. 6 and Supplementary Table S4). Besides Ti, V and Cr are also

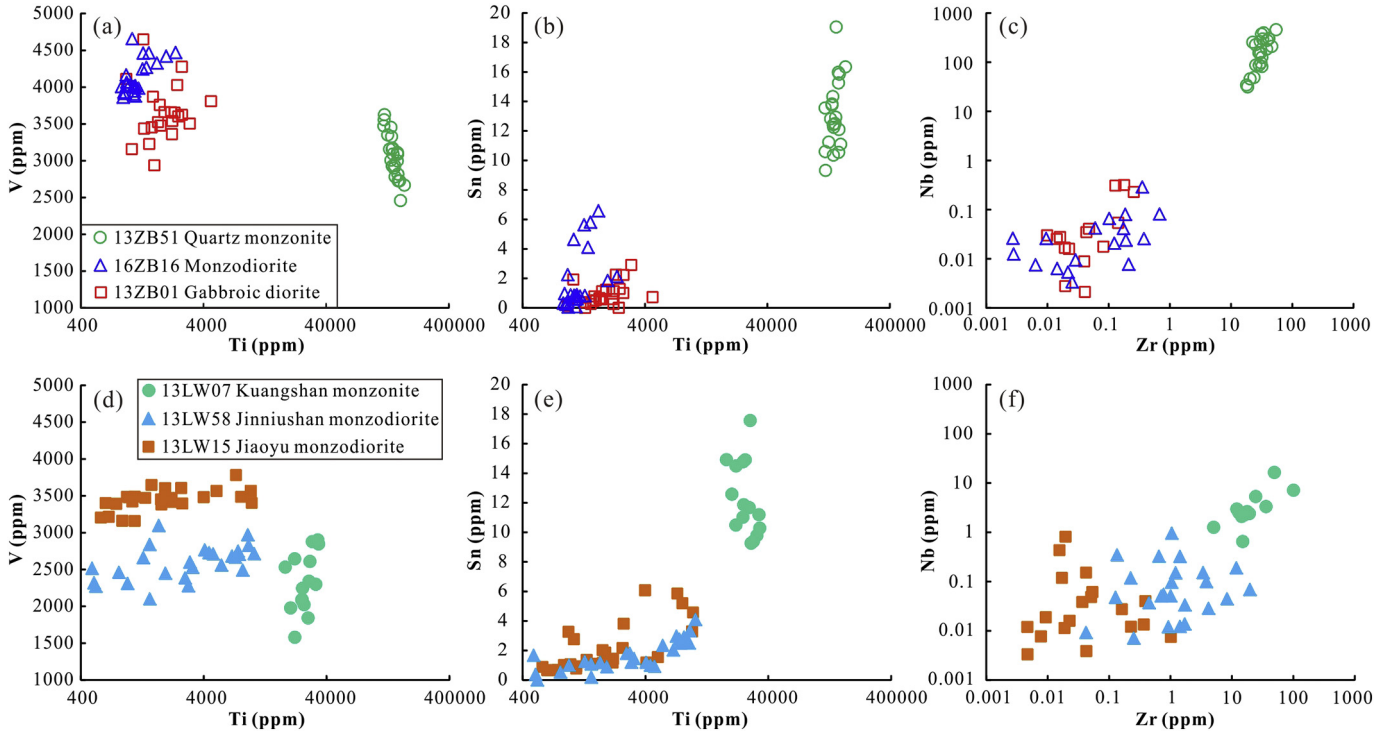

Fig. 6. Plots of V vs. Ti, Sn vs. Ti and Nb vs. Zr for magnetites from the Zibo (a, b and c) and Laiwu (d, e and f) high-Mg diorites.

Table 1
Whole-rock major (wt%) and trace elements (ppm) of the Zibo and Laiwu high-Mg diorites.

Rock-type	Zibo gabbroic diotrite					Zibo monzodiorite				Zibo quartz monzonite			
Sample	13ZB01	13ZB02	13ZB05	13ZB07	13ZB14	16ZB01	16ZB16	16ZB29	16ZB30	13ZB48	13ZB51	13ZB55	13ZB56
SiO_2	55.1	54.4	53.6	54.7	52.5	57.1	57.8	52.9	55.6	65.0	64.4	63.9	64.7
TiO_2	1.04	1.03	0.88	1.01	1.07	1.07	0.96	1.18	1.01	0.57	0.61	0.56	0.56
Al_2O_3	12.9	12.1	12.4	12.8	12.4	14.7	14.4	14.0	14.4	15.4	15.8	15.0	15.2
Fe_2O_3	3.50	3.85	3.50	3.63	3.46	2.95	3.13	3.73	3.43	0.98	1.08	0.40	0.50
FeO	4.69	4.59	5.14	4.84	5.98	4.58	4.56	5.83	5.07	0.89	0.94	0.96	1.18
TFeO	7.84	8.05	8.29	8.11	9.10	7.23	7.38	9.19	8.15	1.77	1.91	1.32	1.63
MnO	0.12	0.13	0.15	0.14	0.14	0.12	0.12	0.15	0.13	0.03	0.03	0.04	0.04
MgO	7.71	8.52	8.51	7.89	8.53	4.98	4.42	5.88	5.08	2.44	2.41	2.79	2.76
CaO	6.40	7.03	8.19	6.71	8.64	6.47	6.07	7.48	6.87	4.30	4.16	5.25	4.89
Na_2O	3.47	3.42	3.01	3.69	3.00	3.76	3.63	3.43	3.59	5.29	5.35	4.66	4.52
K_2O	2.27	2.09	1.96	1.92	1.49	3.03	3.05	2.87	2.91	3.64	3.85	4.80	4.53
P_2O_5	0.37	0.44	0.41	0.39	0.42	0.41	0.34	0.45	0.39	0.20	0.23	0.21	0.20
LOI	0.94	0.72	0.84	0.90	0.87	0.64	0.97	1.18	1.18	0.66	0.70	0.90	0.80
Sum	99.1	98.8	99.1	99.2	99.2	100.4	100.0	99.8	100.2	99.5	99.6	99.6	99.9
Mg#	63.7	65.3	64.7	63.4	62.6	55.1	51.6	53.3	52.6	71.0	69.2	79.0	75.1
Li	18.2	18.1	15.8	16.2	13.6	14.7	14.8	16.8	16.4	10.3	9.5	14.7	14.5
Be	1.10	1.04	1.08	1.07	0.94	2.05	1.84	1.33	1.30	1.79	1.56	1.64	1.73
Sc	20.1	20.4	26.5	20.7	27.8	21.7	19.2	27.1	22.4	8.49	8.23	10.0	9.27
V	165	175	185	168	221	197	165	237	206	45.3	55.8	50.6	71.6
Cr	453	497	449	459	413	149	91.4	134	110	175	193	178	180
Co	33.7	35.7	35.9	34.3	37.2	71.0	72.8	68.8	58.8	6.76	7.21	5.74	7.77
Ni	173	189	137	179	124	58.9	26.2	36.5	30.4	39.3	49.7	39.6	56.2
Cu	45.7	54.5	33.3	48.0	106	31.6	179	123	98.2	28.5	16.7	15.9	6.05
Zn	130	104	109	120	96.3	93.8	76.0	83.8	87.0	34.3	29.1	29.2	23.3
Ga	18.7	17.2	17.5	18.5	17.2	21.2	17.0	18.9	19.3	20.2	21.4	19.1	19.8
Rb	46.5	43.7	42.6	40.4	34.8	74.3	66.4	64.3	64.6	65.5	68.4	92.2	84.1
Sr	667	647	659	695	681	679	538	680	703	640	659	519	654
Cs	1.90	1.57	2.09	1.39	1.47	2.72	1.63	1.41	1.12	1.04	1.08	0.48	0.46
Ba	940	982	726	833	625	1020	783	952	826	1218	1328	1170	1185
Nb	9.70	8.34	7.45	9.35	7.25	12.0	10.3	8.08	8.30	9.31	8.84	8.07	7.51
Ta	0.54	0.52	0.42	0.55	0.43	0.83	0.78	0.54	0.62	0.64	0.41	0.51	0.49
Zr	107	107	131	114	101	177	150	107	137	150	113	189	167
Hf	2.81	2.97	3.50	3.02	2.62	4.51	3.92	2.84	3.60	3.96	2.92	4.58	4.11
Y	17.1	18.0	17.2	17.2	18.3	24.2	19.4	22.6	20.0	10.5	12.4	11.5	10.2
La	25.3	29.0	24.5	25.1	21.8	31.9	23.7	22.4	25.8	27.9	37.8	23.3	24.8
Ce	54.5	62.0	53.7	54.5	47.4	68.2	50.9	50.2	55.5	58.3	82.6	47.7	49.0
Pr	7.37	8.33	7.58	7.41	6.52	8.50	6.36	6.64	6.25	7.16	10.5	6.00	6.01
Nd	28.4	33.0	30.2	28.6	25.9	34.1	25.3	27.9	25.2	26.8	37.1	21.5	22.7
Sm	5.94	7.19	6.53	6.37	6.02	7.11	5.17	5.98	5.80	4.49	6.77	4.13	4.20
Eu	1.82	2.19	1.94	1.84	1.72	1.94	1.40	1.69	1.68	1.61	1.81	1.39	1.09
Gd	5.24	6.35	5.71	5.25	5.19	6.29	4.55	5.49	4.88	3.36	4.60	3.34	3.07
Tb	0.73	0.85	0.78	0.73	0.75	0.87	0.65	0.76	0.69	0.41	0.57	0.45	0.40
Dy	3.56	4.18	3.85	3.67	3.90	4.52	3.52	4.17	3.59	2.03	2.59	2.32	1.96
Ho	0.64	0.73	0.68	0.66	0.72	0.87	0.70	0.82	0.67	0.37	0.48	0.43	0.38
Er	1.69	1.82	1.70	1.68	1.88	2.27	1.87	2.16	1.87	1.01	1.24	1.16	0.98
Tm	0.24	0.24	0.24	0.23	0.27	0.32	0.28	0.31	0.28	0.16	0.18	0.18	0.14
Yb	1.43	1.48	1.48	1.46	1.67	1.99	1.73	1.92	1.76	1.04	1.15	1.15	0.92
Lu	0.21	0.22	0.22	0.22	0.25	0.29	0.25	0.28	0.27	0.16	0.17	0.18	0.14
Tl	0.38	0.28	0.26	0.27	0.20	0.35	0.34	0.45	0.37	0.33	0.33	0.29	0.27
Bi	0.04	0.10	0.17	0.09	0.04	0.04	0.03	0.04	0.03	0.06	0.06	0.05	0.07
Pb	23.1	10.8	10.5	11.5	7.05	11.5	9.4	9.28	11.0	13.7	9.62	7.33	5.23
Th	2.73	3.20	2.96	2.85	2.57	5.95	5.01	3.21	4.09	7.69	5.83	6.63	6.89
U	0.63	0.70	0.80	0.63	0.66	1.41	1.33	0.74	0.99	1.41	1.08	1.18	1.35
Sr/Y	39.0	36.0	38.3	40.5	37.3	28.1	27.7	30.1	35.2	60.7	53.3	44.9	63.9
La/Yb	17.7	19.6	16.6	17.2	13.0	16.0	13.7	11.7	14.7	26.8	32.7	20.3	27.1
δEu	0.97	0.97	0.95	0.95	0.92	0.87	0.86	0.89	0.94	1.21	0.94	1.11	0.88

Rock-type	Laiwu Kuangshan monzonite					Laiwu Jiaoyu monzodiorite					Laiwu Jinniushan monzodiorite				
Sample	13LW02	13LW03	13LW04	13LW07	13LW09	13LW10	13LW11	13LW15	13LW16	13LW17	13LW54	13LW55	13LW56	13LW57	13LW58
SiO_2	57.9	58.3	59.6	60.0	61.2	54.1	54.9	55.0	54.9	56.5	56.6	57.5	56.1	55.1	54.4
TiO_2	0.53	0.58	0.48	0.68	0.53	0.73	0.73	0.83	0.68	0.66	0.55	0.54	0.55	0.55	0.56
Al_2O_3	15.7	15.4	16.2	15.9	16.7	17.0	16.5	15.1	16.1	15.8	14.1	14.1	14.1	13.8	13.4
Fe_2O_3	0.74	0.87	1.07	1.09	0.74	3.76	3.77	3.31	3.01	2.83	4.90	3.63	3.68	3.18	3.33
FeO	1.28	1.22	1.03	1.04	1.15	4.20	4.17	4.69	4.46	4.08	2.93	3.63	3.84	4.51	4.56
TFeO	1.94	2.00	1.99	2.02	1.82	7.59	7.56	7.67	7.17	6.62	7.34	6.89	7.15	7.37	7.56
MnO	0.05	0.06	0.05	0.04	0.05	0.12	0.12	0.13	0.11	0.10	0.14	0.09	0.11	0.12	0.14
MgO	5.76	4.79	4.35	4.31	3.61	4.62	4.48	5.67	5.70	5.00	6.87	6.52	7.32	7.32	7.72
CaO	10.7	9.75	8.72	7.17	7.54	5.08	5.70	6.26	6.60	5.94	4.23	4.44	4.92	5.80	6.13
Na_2O	4.61	5.80	5.30	4.85	5.84	4.95	4.68	3.91	4.12	4.03	4.59	4.62	5.10	4.40	4.38
K_2O	0.93	0.81	1.27	3.20	0.75	2.26	2.24	2.08	1.92	2.26	1.79	2.08	1.73	1.87	1.78
P_2O_5	0.24	0.18	0.22	0.26	0.21	0.31	0.28	0.29	0.27	0.24	0.20	0.19	0.20	0.19	0.19
LOI	1.06	1.58	0.86	0.86	1.32	1.88	1.46	1.60	1.36	1.42	2.96	1.84	1.86	2.08	2.24
Sum	99.6	99.4	99.3	99.5	99.8	99.5	99.5	99.3	99.7	99.3	100.2	99.6	100.0	99.3	99.4

Table 1 (*continued*)

Rock-type	Laiwu Kuangshan monzonite					Laiwu Jiaoyu monzodiorite					Laiwu Jinniushan monzodiorite				
Sample	13LW02	13LW03	13LW04	13LW07	13LW09	13LW10	13LW11	13LW15	13LW16	13LW17	13LW54	13LW55	13LW56	13LW57	13LW58
Mg#	84.1	81.0	79.6	79.1	78.0	52.0	51.4	56.9	58.6	57.4	62.5	62.8	64.6	63.9	64.5
Li	28.4	29.2	14.2	21.4	20.8	24.9	26.4	21.6	20.1	14.6	20.4	19.1	15.0	14.0	13.6
Be	1.23	1.30	1.30	1.40	1.29	1.24	1.20	1.14	1.08	1.16	0.95	0.94	0.90	0.85	0.80
Sc	22.2	20.0	17.6	18.1	14.8	21.6	22.6	22.9	21.9	19.0	22.9	21.2	22.8	23.0	24.0
V	76.1	90.7	74.5	70.9	54.8	160	188	178	163	157	147	141	148	155	158
Cr	414	259	197	252	219	79.0	80.1	206	243	227	381	354	355	427	456
Co	8.44	9.85	8.15	6.16	7.89	21.2	22.6	25.3	25.0	23.1	28.3	26.8	30.0	31.1	32.3
Ni	53.6	46.4	37.3	39.8	38.2	18.2	24.7	51.1	54.8	52.1	86.8	78.3	89.7	87.3	92.4
Cu	7.94	18.4	9.64	3.83	20.1	57.3	45.3	97.5	61.7	37.0	95.3	17.7	6.40	61.6	82.8
Zn	18.3	30.0	11.1	11.2	34.5	65.6	60.8	59.2	63.8	52.7	64.4	41.9	41.8	53.5	58.0
Ga	17.6	16.8	19.2	18.4	18.1	20.1	20.4	18.6	19.5	18.8	16.6	15.9	15.9	15.9	15.6
Rb	22.5	16.3	27.5	51.4	24.2	45.1	47.2	41.6	39.8	48.8	34.2	40.2	32.1	34.5	29.2
Sr	794	717	729	586	745	673	672	573	634	550	228	369	311	399	328
Cs	0.69	0.56	1.11	1.03	0.65	1.07	0.61	1.53	1.46	2.24	0.14	0.19	0.16	0.13	0.09
Ba	495	219	536	1106	324	836	815	772	966	1036	379	878	657	870	801
Nb	4.32	5.37	5.33	6.86	4.49	5.15	5.25	5.75	4.30	5.72	3.83	3.89	3.66	3.66	3.55
Ta	0.28	0.29	0.29	0.36	0.29	0.26	0.27	0.30	0.23	0.31	0.22	0.22	0.20	0.21	0.21
Zr	125	112	107	166	149	137	131	101	89.5	138	82.5	85.4	81.2	84.8	82.9
Hf	3.06	2.82	2.69	4.11	3.58	3.23	3.20	2.88	2.26	3.56	2.15	2.23	2.12	2.23	2.21
Y	12.2	12.0	12.1	16.2	15.0	16.9	15.8	18.6	14.2	14.8	11.8	10.8	10.9	11.7	11.2
La	17.4	18.4	23.5	27.0	28.3	24.8	23.6	23.9	23.2	25.9	17.9	14.5	15.3	15.5	20.9
Ce	29.4	36.9	48.8	32.4	53.4	51.0	48.0	50.6	46.3	51.4	34.9	26.5	29.3	31.6	36.8
Pr	3.64	4.60	6.10	4.73	8.38	6.86	6.36	6.92	6.04	6.58	4.44	3.64	3.89	4.30	4.54
Nd	14.1	17.9	22.7	18.7	32.1	28.0	23.8	27.1	23.0	23.9	16.6	13.8	14.8	17.0	16.8
Sm	2.96	3.33	3.81	4.06	4.94	5.20	5.13	5.70	4.47	4.66	3.64	3.04	3.37	3.58	3.47
Eu	1.10	1.05	1.42	1.29	1.78	1.59	1.51	1.64	1.31	1.28	1.06	1.06	1.05	1.20	1.17
Gd	2.46	2.82	3.16	3.59	4.15	4.32	4.11	4.83	3.82	3.94	3.03	2.69	2.75	3.14	3.00
Tb	0.37	0.40	0.43	0.53	0.53	0.61	0.58	0.69	0.54	0.55	0.44	0.40	0.40	0.45	0.43
Dy	2.16	2.25	2.25	2.94	2.71	3.28	3.09	3.72	2.88	2.96	2.39	2.14	2.30	2.41	2.44
Ho	0.43	0.43	0.44	0.59	0.53	0.65	0.62	0.71	0.56	0.58	0.46	0.43	0.45	0.47	0.46
Er	1.14	1.16	1.22	1.70	1.44	1.80	1.63	1.95	1.54	1.62	1.29	1.14	1.17	1.30	1.21
Tm	0.17	0.17	0.18	0.25	0.20	0.27	0.25	0.29	0.24	0.25	0.20	0.17	0.17	0.19	0.18
Yb	1.09	1.12	1.19	1.67	1.26	1.72	1.56	1.84	1.50	1.61	1.28	1.10	1.12	1.22	1.17
Lu	0.17	0.16	0.18	0.27	0.20	0.27	0.24	0.27	0.23	0.25	0.20	0.17	0.17	0.19	0.18
Tl	0.10	0.09	0.24	0.17	0.10	0.23	0.24	0.20	0.22	0.25	0.13	0.14	0.10	0.11	0.11
Bi	0.03	0.17	0.03	0.04	0.26	0.04	0.00	0.00	0.00	0.00	0.03	0.04	0.04	0.08	0.12
Pb	6.49	3.98	6.30	3.96	5.31	8.40	5.25	7.22	9.64	8.07	11.2	3.79	0.19	5.24	1.12
Th	3.86	3.45	4.14	5.61	4.10	3.19	2.75	2.77	2.97	3.34	2.47	2.72	2.32	2.48	2.25
U	0.56	1.14	0.97	1.09	0.77	0.78	0.79	0.74	0.53	0.89	0.49	0.58	0.48	0.53	0.55
Sr/Y	65.2	59.7	60.3	36.2	49.8	39.9	42.6	30.8	44.6	37.3	19.4	34.1	28.5	34.0	29.3
La/Yb	16.0	16.4	19.8	16.2	22.4	14.4	15.2	13.0	15.5	16.1	14.0	13.2	13.6	12.7	17.9
δEu	1.21	1.03	1.21	1.01	1.17	1.00	0.97	0.93	0.90	0.89	0.95	1.11	1.02	1.07	1.08

LOI: loss on ignition. Mg# = 100 × Mg / (Mg + ∑Fe) molar ratio.

enriched in the magnetite, with concentrations commonly higher than 1000 ppm (Supplementary Table S4). Magnesium, Al, Si and Mn are less enriched, which show concentrations varying from several hundreds to thousands of ppm. Cobalt, Ni, Zn and Ga show the concentrations of tens to hundreds of ppm. Germanium, Sc, Sn and Mo also occur, the concentrations of which are commonly <10 ppm. Notably, the strongly mineralized intrusions have the highest Mg, Si, Sc, Sn, Zr and Nb but the lowest V, Co and Mo concentrations (Fig. 6 and Supplementary Table S4). The concentrations of P, Ca, Na and K, which can be easily affected by mineral inclusions (e.g., apatite) and/or fluid inclusions, commonly vary widely. Generally, the trace elements of magnetite show larger variations in the Laiwu intrusions than in the Zibo intrusions.

4.5. Whole-rock major and trace elements

The high-Mg diorites in the Zibo and Laiwu areas show wide variations in major elements, having SiO_2 contents of 52.5–65.0 wt%, MgO contents of 2.41–8.53 wt%, TFeO contents of 1.32–9.19 wt%, CaO contents of 4.16–10.7 wt%, and $Na_2O + K_2O$ contents of 4.49–9.46 wt% (Table 1). Nonetheless, the Mg# values of all the rocks are higher than 50 (51–84), consistent with the features of high Mg# andesites (SiO_2 > 54 wt%, Mg# > 50) defined by Kelemen et al. (2003). They are classified into gabbro-diorite to quartz monzonite in the SiO_2 vs. $Na_2O + K_2O$ discrimination diagram (Fig. 7a), and are chemically metaluminous and calc-alkaline (Fig. 7b and c). It is noted that both the strongly mineralized intrusions in the Zibo and Laiwu areas are the most felsic ones, having the highest SiO_2 and $Na_2O + K_2O$ and the lowest TFeO, MgO and MnO contents (Table 1). In addition, they show remarkably high Mg# values (69–84) with drastic decrease of TFeO contents and TFeO/MgO ratios.

All the rocks have similar trace element and REE distribution patterns. They are depleted in high field strength elements (HFSEs, such as Nb, Ta, Zr, P and Ti) and enriched in large ion lithophile elements (LILEs, such as Sr and Ba) on the Primitive Mantle-normalized spidergram, and show enrichment in LREEs and depletion in HREEs on the Chondrite-normalized REE distribution diagram (Fig. 8). In addition, compared with the ore-barren intrusions, the strongly mineralized intrusions have stronger fractionation between the LREEs and the HREEs and higher Sr/Y ratios (36–65). Combined with their high Sr (519–794 ppm) and low Y (10.2–16.2 ppm) and Yb (0.92–1.67 ppm) concentrations, the strongly mineralized intrusions show similar geochemical features to those of adakites (Sr > 400 ppm, Y ≤ 18 ppm, Yb ≤ 1.9 ppm, Sr/Y > 20, Castillo, 2012; Defant and Drummond, 1990) (Fig. 9a), but their La/Yb ratios (16–33) are commonly lower (Fig. 9b).

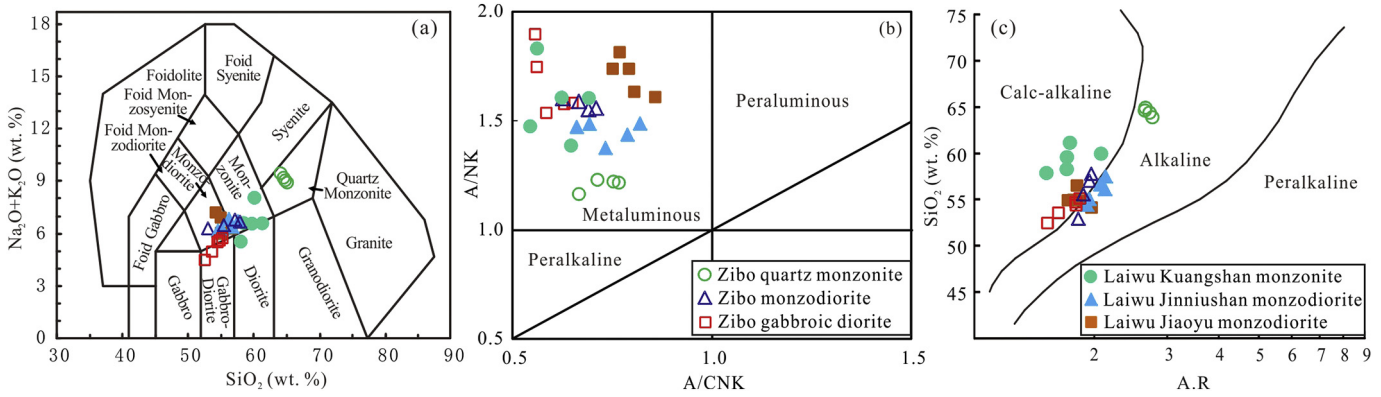

Fig. 7. Plots of ($Na_2O + K_2O$) vs. SiO_2 (a), A/NK vs. A/CNK [A/NK = molar ratio $Al_2O_3/(Na_2O + K_2O)$, A/CNK = molar ratio $Al_2O_3/(CaO + Na_2O + K_2O)$] (b) and SiO_2 vs. A.R. [A.R. = $(Al_2O_3 + CaO + Na_2O + K_2O)/(Al_2O_3 + CaO\text{-}Na_2O\text{-}K_2O)$] (c) for the Zibo and Laiwu high-Mg diorites. (a) and (c) are modified from Middlemost (1994) and Wright (1969), respectively.

4.6. Whole-rock Sr-Nd-Pb isotopic compositions

The Sr-Nd-Pb isotopic compositions of the high-Mg diorites are shown in Table 3, Figs. 10 and 11.

For the Zibo high-Mg diorites, the most mafic ore-barren gabbroic diorite has the lowest $(^{87}Sr/^{86}Sr)_i$ (0.704726–0.704875), the highest $\varepsilon_{Nd}(t)$ (−6.4 to −5.4) and the lowest Pb isotopic compositions ($(^{208}Pb/^{204}Pb)_i$ = 37.087–37.115, $(^{207}Pb/^{204}Pb)_i$ = 15.348–15.353, $(^{206}Pb/^{204}Pb)_i$ = 17.110–17.143). The moderately mineralized monzodiorite and the strongly mineralized quartz monzonite do not show significant difference in $(^{87}Sr/^{86}Sr)_i$, but the Nd and Pb isotopic compositions are a little bit higher and lower respectively in the quartz monzonite. The $(^{87}Sr/^{86}Sr)_i$, $\varepsilon_{Nd}(t)$, $(^{208}Pb/^{204}Pb)_i$, $(^{207}Pb/^{204}Pb)_i$ and $(^{206}Pb/^{204}Pb)_i$ are 0.705761–0.705974, −9.5 to −8.6, 37.317–37.754, 15.367–15.444 and 17.123–17.629 in the monzodiorite while in the quartz monzonite are 0.705585–0.706058, −8.2 to −7.7, 37.059–37.364, 15.404–15.445 and 17.308–17.410.

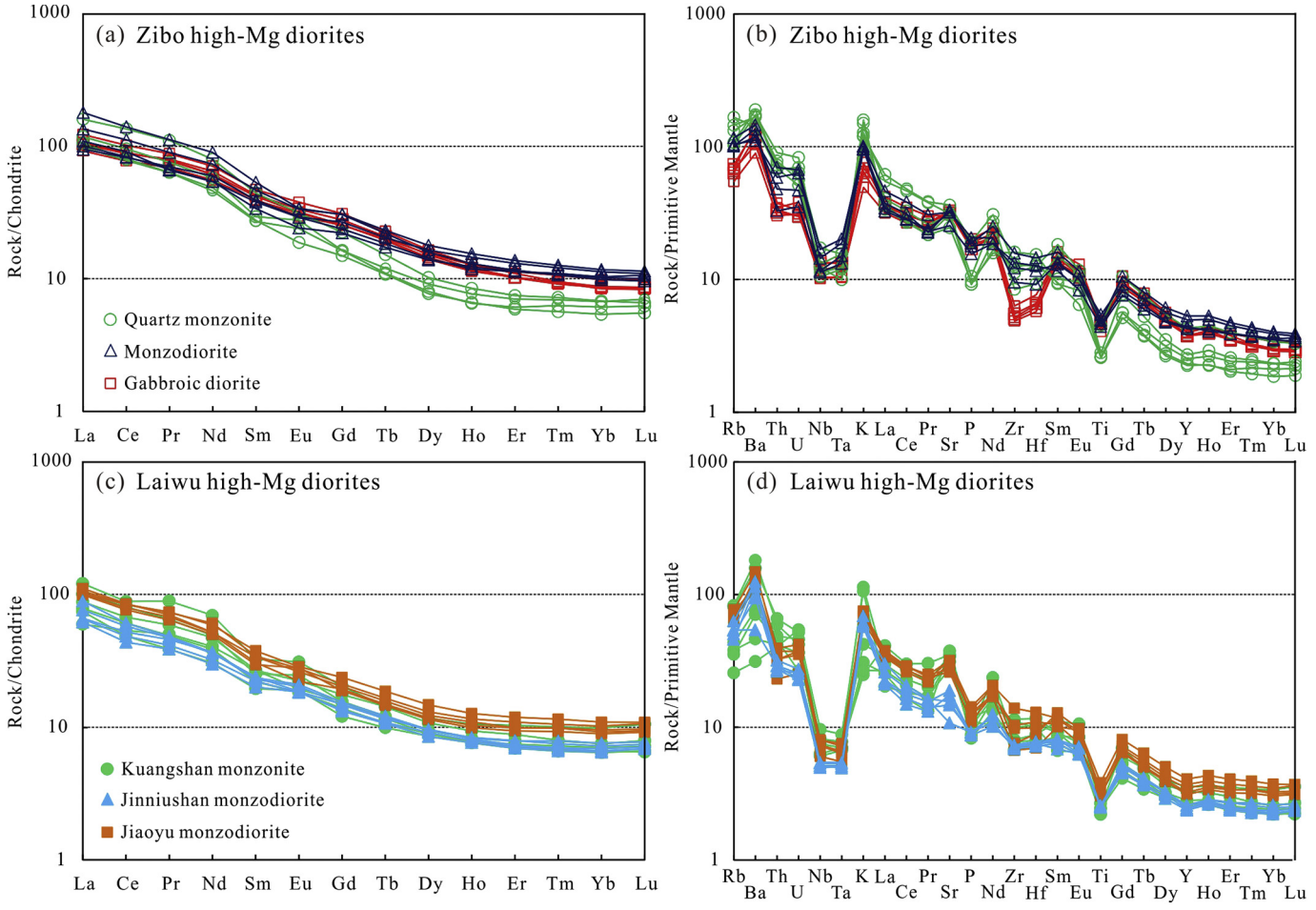

Fig. 8. Chondrite-normalized REE distribution patterns and Primitive Mantle normalized spider diagrams for the Zibo (a and b) and Laiwu (c and d) high-Mg diorites. Chondrite and Primitive Mantle values are from Sun and McDonough (1989).

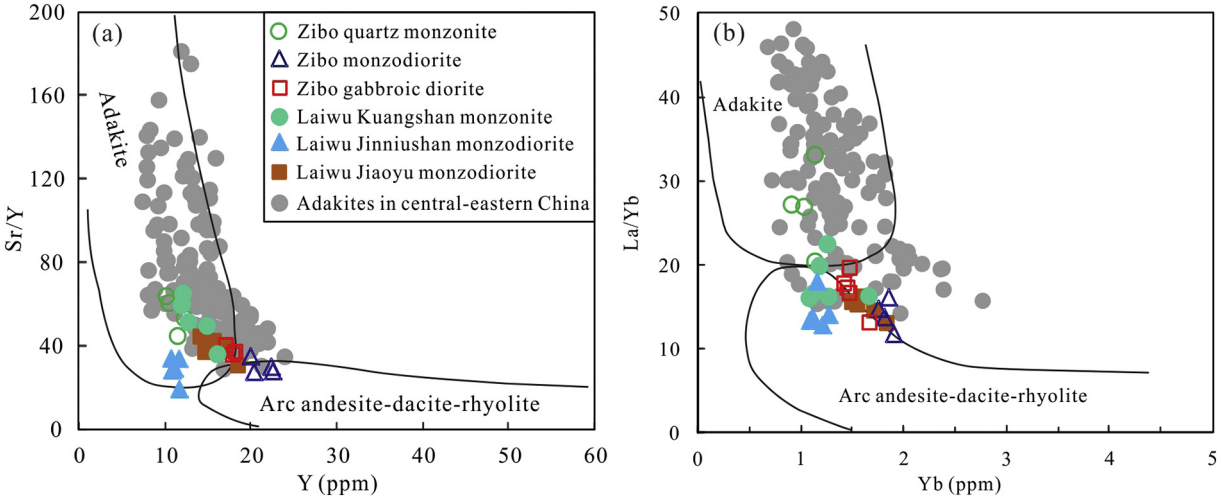

Fig. 9. Plots of Sr/Y vs. Y (a) and La/Yb vs. Yb (b) for the Zibo and Laiwu high-Mg diorites (modified after Castillo, 2012). The data of the adakites in central-eastern China are from S.A. Liu et al. (2010) and references therein.

For the Laiwu high-Mg diorites, from the ore-barren Jiaoyu and Jinniushan monzodiorites to the strongly mineralized Kuangshan monzonite, the $(^{87}Sr/^{86}Sr)_i$ shows a slight increase, varying from 0.706259–0.706824 to 0.706994–0.707125 and to 0.707223–0.707507. The Jiaoyu intrusion has the lowest Nd and Pb isotopic compositions, showing the $\varepsilon_{Nd}(t)$ of −16.0 to −15.5, $(^{208}Pb/^{204}Pb)_i$ of 36.306–36.527, $(^{207}Pb/^{204}Pb)_i$ of 15.205–15.259 and $(^{206}Pb/^{204}Pb)_i$ of 16.334–16.609, respectively. The Kuangshan intrusion has moderate Nd ($\varepsilon_{Nd}(t)$ = −15.8 to −14.8) and Pb ($(^{208}Pb/^{204}Pb)_i$ = 37.115–37.193, $(^{207}Pb/^{204}Pb)_i$ = 15.327–15.347, $(^{206}Pb/^{204}Pb)_i$ = 16.883–16.986) isotopic compositions, while those in the Jinniushan intrusion ($\varepsilon_{Nd}(t)$ = −15.2 to −14.8, $(^{208}Pb/^{204}Pb)_i$ = 37.195–37.529, $(^{207}Pb/^{204}Pb)_i$ = 15.405–15.418, $(^{206}Pb/^{204}Pb)_i$ = 17.517–17.597) are the highest.

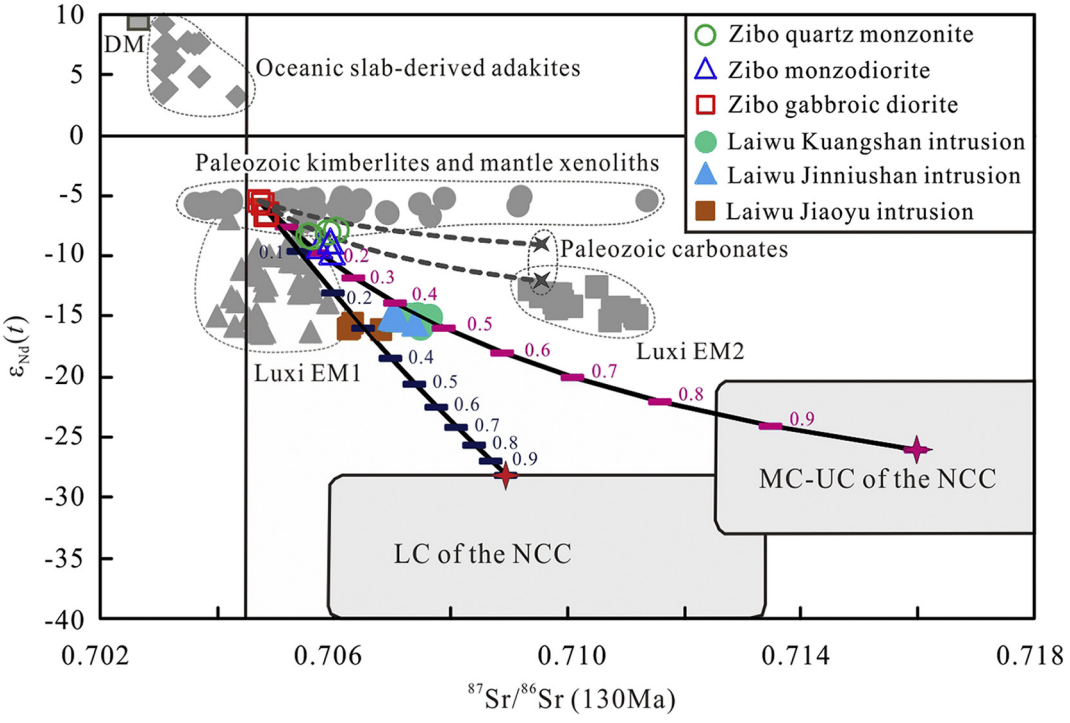

Fig. 10. Diagram of initial $(^{87}Sr/^{86}Sr)_i$ vs. $\varepsilon_{Nd}(t)$ for the Zibo and Laiwu high-Mg diorites. The early Cretaceous EM1 is defined by the Jinan and Zouping basalts/gabbros in the northwestern Luxi Block, the Sr-Nd isotopic data of which are from Guo et al. (2003), Li et al. (2007), D.B. Yang et al. (2012) and Q.L. Yang et al. (2012). The EM2 is defined by the Yinan, Fangcheng and Feixian basalts/gabbros in the southeastern Luxi Block, and the data are from Xu et al. (2004b), D.B. Yang et al., 2012 and Zhang et al. (2002). The fields of lower and upper crusts of the NCC are modified from Jahn et al. (1999). The intermediate granulite (DMP-27) in the Hannuoba area of eastern NCC is selected to represent the lower crust (Y.S. Liu et al., 2004). The data of Paleozoic kimberlites and mantle xenoliths in the Mengyin area are from Yang et al. (2009) and Zheng and Lu (1999). The Sr-Nd isotopic data of Paleozoic carbonates are from J.M. Liu et al. (2004). The oceanic slab-derived adakites represent partial melts of oceanic slabs, the data of which are from Aguillo'n-Robles et al. (2001), Deng et al. (2017), Lázaro and García-Casco (2008) and Sajona et al. (2000). The mixing modelling parameters are Sr = 681 ppm, $^{87}Sr/^{86}Sr$ = 0.70473, Nd = 42 ppm, ε_{Nd} = −5.4 for the EM1 (represented by the 13ZB14 in this study), Sr = 1122 ppm, $^{87}Sr/^{86}Sr$ = 0.70897, Nd = 49.5 ppm, ε_{Nd} = −28.1 for the lower crust (Y.S. Liu et al., 2004, J.M. Liu et al., 2004), Sr = 250 ppm, $^{87}Sr/^{86}Sr$ = 0.716, Nd = 26 ppm, ε_{Nd} = −26 for the middle-upper crust of the NCC (Wang et al., 2006), and Sr = 245 ppm, $^{87}Sr/^{86}Sr$ = 0.7095, Nd = 22 ppm, ε_{Nd} = −12 to −9 for the Paleozoic carbonates (Gao et al., 1998; J.M. Liu et al., 2004; Liu et al., 2018). Symbols as in Fig. 9.

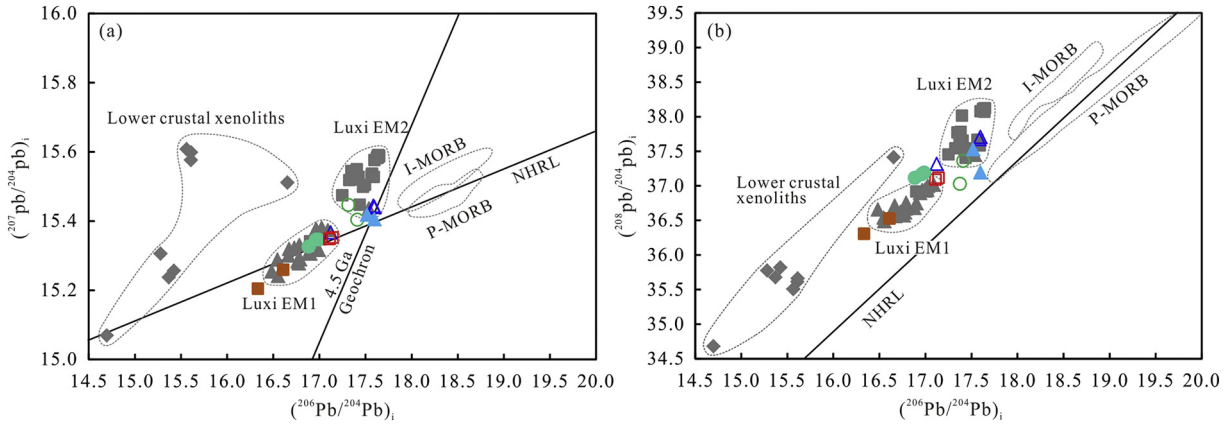

Fig. 11. Initial $(^{207}Pb/^{204}Pb)_i$ vs. $(^{206}Pb/^{204}Pb)_i$ (a) and $(^{208}Pb/^{204}Pb)_i$ vs. $(^{206}Pb/^{204}Pb)_i$ (b) for the Zibo and Laiwu high-Mg diorites. The EM1 in Luxi Block is defined by the Jinan and Zouping basalts/gabbros (Li et al., 2007; D.B. Yang et al., 2012), whereas the EM2 is defined by the Fangcheng, Yinan and Feixian basalts/gabbros (Zhang et al., 2002; Xu et al., 2004b; D.B. Yang et al., 2012). Isotopic data of lower crustal xenoliths in the eastern NCC are from Ying et al. (2010). The fields of I-MORB (Central Indian MORB) and P-MORB (Pacific MORB) are from Zou et al. (2000). NHRL (Northern Hemisphere Reference Line) and 4.55 Ga geochron are from Zindler and Hart (1986). Symbols as in Fig. 9.

The Laiwu intrusions have much lower $\varepsilon_{Nd}(t)$ and higher $(^{87}Sr/^{86}Sr)_i$ values than those of the Zibo intrusions (Fig. 10). In addition, the $\varepsilon_{Nd}(t)$ values are more uniform in the Laiwu intrusions.

5. Discussion

Field investigations and zircon U-Pb dating suggest that no matter the different lithologies of the Jinling intrusive complex in the Zibo area or the different intrusions in the Laiwu area, the ore-barren and the ore-bearing high-Mg dioritic rocks are closely spatially and temporally associated. Especially, the strongly mineralized rocks are more felsic and younger than those of the ore-barren rocks. This implies that the ore-bearing rocks might be genetically related to the ore-barren rocks. Then, did the ore-barren and ore-bearing rocks share the same or similar magma source? Whether or not special source materials or magmatic processes (e.g., magma mixing, MASH and AFC) were required for the ore-forming magmas?

Following, we explore the potential sources, magmatic processes, physicochemical conditions and geodynamic regime that might be favorable for generating the high-Mg diorites and the associated Fe mineralization.

5.1. The magma sources

5.1.1. Mantle source

Regardless of ore-barren or ore-bearing, all the diorites in the Zibo and Laiwu areas show high Mg# values (>51), basically higher than those of the partial melts from basalts at similar silica contents (Fig. 12a). This likely indicates the involvement of mantle peridotite or mantle peridotite-derived melts in the magma source. Actually, the most mafic rocks of them (e.g., the gabbroic diorite in the Zibo and the Jinniushan monzodiorite in the Laiwu areas) have high Cr and Ni concentrations up to 354–497 ppm and 78–189 ppm, respectively, which are comparable to those of the nearby mantle-derived Jinan gabbros and the primitive MORB and arc basalts worldwide (Fig. 12b). More importantly, all the rocks show Sr, Nd and Pb isotopic compositions distinct from those of the lower and upper crusts of the NCC, but close to the contemporary mantle-derived basalts/gabbros in the study region (Figs. 10 and 11). These features, therefore, strongly support the derivation of the high-Mg diorites mainly from the subcontinental lithospheric mantle (SCLM), although the mineralized intrusions seem to have undergone more magmatic processes (e.g., crustal assimilation and/or fractional crystallization). Other potential ways to generate the high-Mg diorites, such as

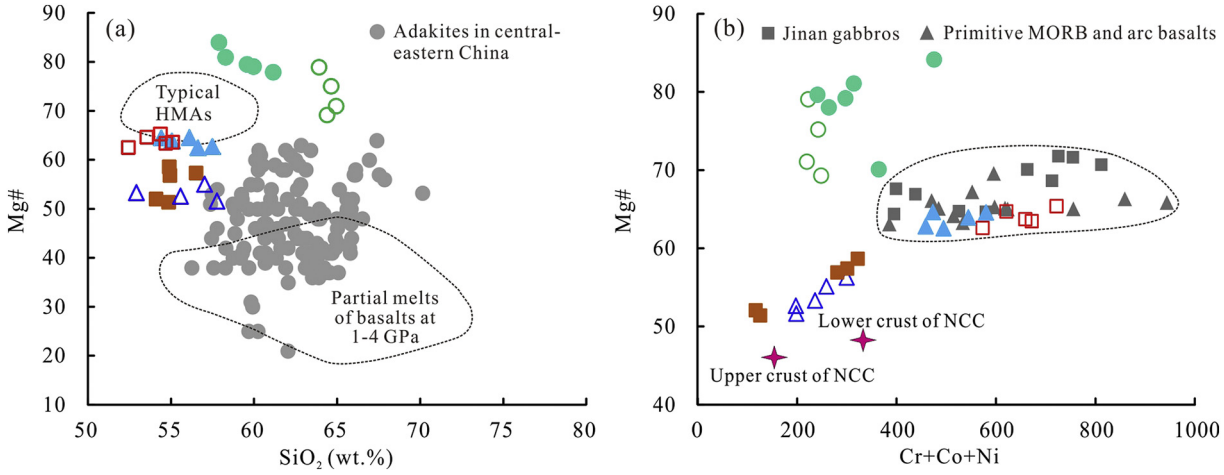

Fig. 12. Plots of Mg# vs. SiO_2 (a) and Mg# vs. Cr + Co + Ni (b) for the Zibo and Laiwu high-Mg diorites. In (a), the fields of HMAs and partial melts of basalts are from Rapp et al. (1999). The plots of adakites in central-eastern China (S.A. Liu et al., 2010) are also shown for comparison. In (b), the data of primitive MORB and arc basalts and Jinan gabbros are from Kelemen et al. (2003) and Q.L. Yang et al. (2012), respectively, while those of the lower and upper crusts of the NCC are from Gao et al. (1998). Symbols of high-Mg diorites as in Fig. 9.

delaminated continental lower crust-derived or subducted oceanic slab-derived melts interacting with mantle peridotite, can be precluded, mainly due to the following reasons: (1) the Luxi Block was located far away from the Paleo-Pacific subduction zone during the early Cretaceous (>1000 km, Maruyama et al., 1997; Zhou and Li, 2000; Xu et al., 2004a). It would be almost impossible for the slab-derived melts to pass through the thick mantle wedge (probably >400 km, Xu et al., 2011; Liu et al., 2017); (2) the Luxi Block suffered intense extension during the early Cretaceous (Zhang et al., 2007), the tectonic setting of which could not lead to the lower crust delamination at that time. Continental collision between the NCC and the SCB, which has the potential to cause lower crust delamination, occurred at the Triassic (Li et al., 1993; Meng and Zhang, 1999), about 100 Ma years earlier than the emplacement of the high-Mg diorites; (3) the mafic end-members of the high-Mg diorites have obviously high Mg#, Cr and Ni values, which are similar to those of the primitive basaltic melts but distinct from the melts derived from the continental or oceanic crust (Fig. 12); (4) most of the Zibo and Laiwu high-Mg diorites show Sr/Y and La/Yb ratios, especially the La/Yb ratios, lower than those of the typical slab-derived adakites and the adakitic rocks derived from continental or oceanic crust in the central-eastern China (Fig. 9); (5) the isotopic compositions of the high-Mg diorites are neither similar to the lower crust nor close to the oceanic slab (Figs. 10 and 11); (6) recycled oceanic slab materials were just detected in the mantle enclaves/magmas younger than ~100 Ma in the eastern NCC (Zhu et al., 2012; Xu, 2014).

It is notable that all the high-Mg diorites are characterized by arc-like geochemistry (Fig. 8) and low $\varepsilon_{Nd}(t)$ values (Fig. 10), which indicate that the SCLM source probably had been metasomatized. Previous studies showed that the early Cretaceous gabbros/basalts as well as the mantle peridotite enclaves in the study region also show such features (Zhang et al., 2002; Xu et al., 2004b; Xu et al., 2008), corroborating the mantle metasomatism. The puzzling question is that when and how the SCLM was metasomatized. The Sr-Nd isotopic compositions of the Zibo gabbroic diorite not only resemble those of the most “depleted” gabbros in the study region, but also overlap the nearby Paleozoic Mengyin kimberlites and mantle xenoliths (~470 Ma, Yang et al., 2009) (Fig. 10). This implies that the gabbroic diorite might be the “pure” product of the SCLM melting without significant crustal contamination and thus can denote the primary isotopic compositions of the Mesozoic SCLM. In addition, it also implies that the Mesozoic SCLM beneath the study region might be directly inherited from the Paleozoic SCLM with minor isotopic modification. If it is true, the mantle metasomatism might be a long-term metasomatism (Guo et al., 2001, 2003), occurring during or before the Paleozoic. This inference is supported by the geochemistry of the Paleozoic kimberlites and mantle xenoliths, which also shows enrichment in REEs, strong fractionation between LREEs and HREEs, and high Sr and low Nd isotopic compositions (Zheng and Lu, 1999; Chu et al., 2009; Yang et al., 2009). Considering the NCC remained largely stable after the ca. 1.8 Ga (Zhai and Santosh, 2011; Zhao et al., 2012), the mantle metasomatism was probably related to the remarkable amalgamation between the eastern and western blocks of the NCC during the ca. 1.9–1.8 Ga (Zhao et al., 2012), as also inferred by other researchers (e.g., Gao et al., 2002; Huang et al., 2012).

It should be pointed out that, however, the Paleozoic SCLM has been proved to be refractory (Zheng et al., 2001; Gao et al., 2002; Chu et al., 2009), contradicting the fact that the Mesozoic SCLM beneath the southeastern NCC was obviously hydrous during the early Cretaceous (containing>1000 ppm H_2O, Xia et al., 2013; Liu and Xia, 2014). The abundant occurrence of amphibole and/or biotite in the high-Mg diorites also supports the mantle source being hydrous. This implies that something should have happened between the Paleozoic and the Mesozoic, leading to the hydration of the Mesozoic SCLM. The Triassic northward continental subduction of the SCB beneath the southern NCC has been considered to modify the SCLM of the NCC significantly (e.g., Guo et al., 2003; Zhang et al., 2002; Xu et al., 2004a, 2004b; Huang et al., 2012; D.B. Yang et al., 2012; Q.L. Yang et al., 2012; Xu et al., 2013). However, based on numerous isotopic studies on mantle-derived rocks, such modification was confined within a distance no >300 km from the subduction zone (e.g., D.B. Yang et al., 2012; Q.L. Yang et al., 2012). The Sr-Nd-Pb isotopic compositions of the high-Mg diorites in this study are distinct from those of the SCB-modified EM2 (Figs. 10 and 11), indicating that the SCLM beneath the study region had not been significantly affected by such modification. Previous subduction of the Paleo-Tethyan Oceanic Plate between the NCC and the SCB, which had been accomplished before the continental collision (Meng and Zhang, 1999), might contribute to the hydration of the SCLM. However, no robust evidence has been found so far to support such effect. An early Jurassic asthenosphere-derived alkaline intrusion (~180 Ma) was identified in the Luxi Block, which does not show any slab modification in its mantle source (Zhang et al., 2005; Lan et al., 2012). More possibly, it is noted that the Paleo-Pacific Plate strongly subducted underneath the eastern Asian continent during the Mesozoic (Maruyama et al., 1997; Sun et al., 2007). Based on compiling and examining petrochemical characteristics of drilled basalts, Komiya and Maruyama (2007) concluded that the western Pacific region is the place where abundant water contents have been transported into the mantle during the last 150 Ma. Windley et al. (2010) evaluated the effects of the westward subduction of the Paleo-Pacific Oceanic Plate on transferring water into the deep mantle, concluding that the mantle transition zone (410–660 km depth) under the eastern NCC should be highly enriched in water due to the stagnant slab releasing water into the overlying mantle. Experiments and simulations have proven that considerable amounts of water can be transported by old, cold oceanic lithosphere into the mantle transition zone (Maruyama and Okamoto, 2007). Geophysical studies directly indicate that a stagnant oceanic slab is being situated in the transition zone beneath the eastern Asian continent (Xu et al., 2011; Liu et al., 2017; Zhao et al., 2017). These results, therefore, suggest that the Paleo-Pacific Oceanic Plate might do not provide melts for the high-Mg diorites, but the slab-released water hydrating the mantle likely occurred.

In conclusion, the Mesozoic SCLM beneath the study region had been anciently metasomatized and recently hydrated, becoming the favorable source for the high-Mg diorites.

5.1.2. Crustal involvement

The Sr-Nd isotopic compositions of the high-Mg diorites vary largely from the Zibo to the Laiwu area, and show some trends from the EM1 to the lower or upper crust (Fig. 10), indicating that various crustal involvement should have occurred. The presence of captured zircons with late Archean to early Paleoproterozoic ages in these rocks (e.g., the Zibo quartz monzonite and the Laiwu Jinniushan intrusion) provides the direct evidence for crustal involvement (Fig. 4). In order to constrain which and how the crustal materials were involved in, magma mixing modelling based on Sr-Nd isotopes was applied using the method of Langmuir et al. (1978). The Zibo gabbroic diorite (13ZB14) is selected to represent the SCLM because it has the most primitive geochemical and isotopic compositions. The modelling indicates that lower crust could not be responsible for the crustal involvement in the Zibo monzodiorite and quartz monzonite, mainly due to its distinctly low Sr and Nd isotopic compositions (Fig. 10). Alternatively, assimilation of ~20% middle-upper crustal materials into the SCLM-derived melts can well generate the isotopic features of the monzodiorite (Fig. 10). The monzodiorite was probably evolved from the gabbroic diorite through continuous middle-upper crustal assimilation, as indicated by the excellent correlation between $(^{87}Sr/^{86}Sr)_i$ and $\varepsilon_{Nd}(t)$ as well as between MgO and $\varepsilon_{Nd}(t)$ from the gabbroic diorite to the

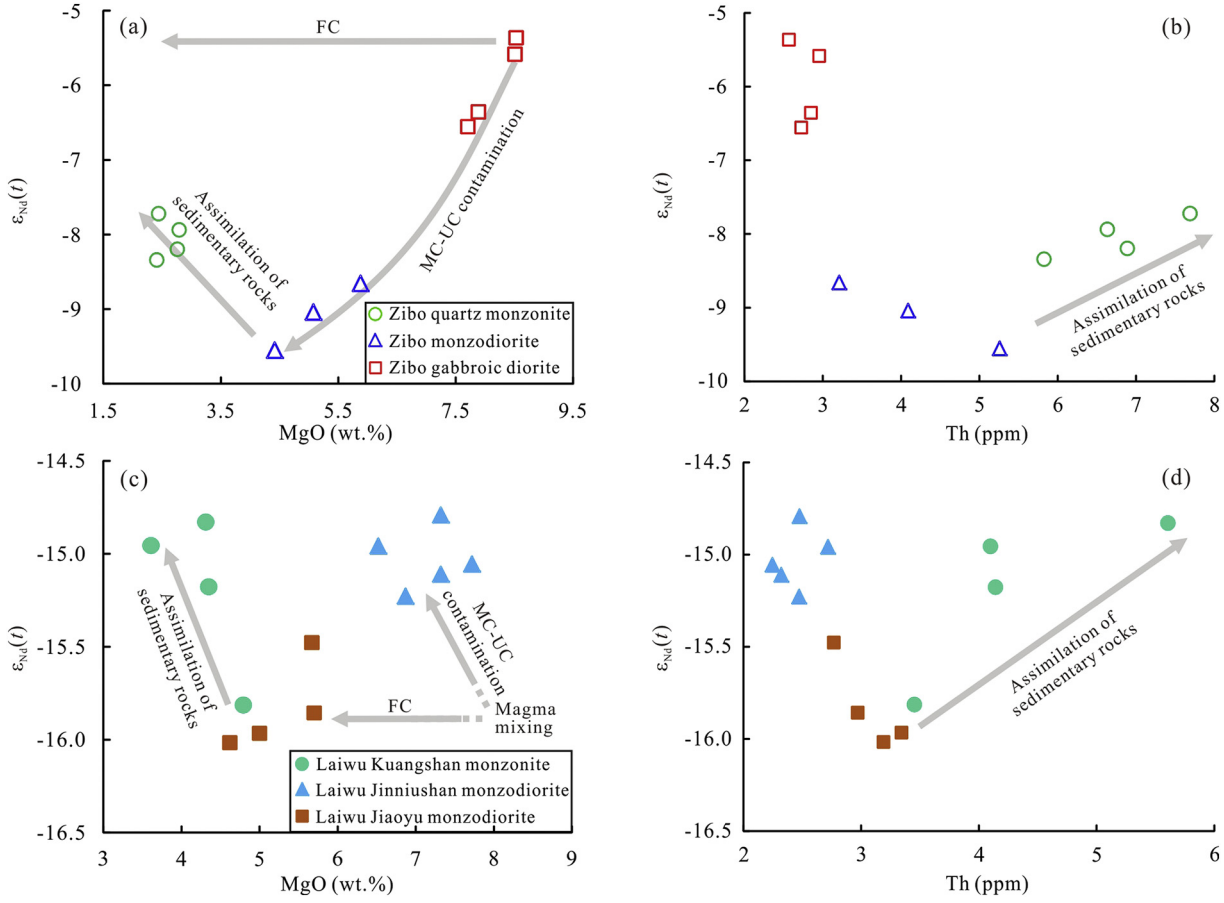

Fig. 13. Plots of $\varepsilon_{Nd}(t)$ vs. MgO and $\varepsilon_{Nd}(t)$ vs. Th for the Zibo (a and b) and Laiwu (c and d) high-Mg diorites. FC-fractional crystallization, MC-middle crust, UC-upper crust. Sedimentary rocks are composed mainly of carbonate rocks.

monzodiorite (Figs. 10 and 13a). The more felsic quartz monzonite, however, seems not to be evolved from the gabbroic diorite or the monzodiorite through such assimilation. It is noted that the quartz monzonite has higher $\varepsilon_{Nd}(t)$ values than the more mafic monzodiorite (Fig. 13a). Combined with the $\varepsilon_{Nd}(t)$ showing positive correlation with $(^{87}Sr/^{86}Sr)_i$ in the quartz monzonite (Fig. 10), another source more enriched in radiogenic Nd should be assimilated in this rock. The upper crust in the study region is composed mainly by a basement of Archean to early Paleoproterozoic TTG gneisses and a cover of Paleozoic sedimentary rocks (mainly carbonates interbedded with shales and sandstones), of which the TTG gneisses have $\varepsilon_{Nd}(t)$ values commonly lower than −20 (Jahn et al., 1988). The magma mixing modelling shows that assimilation of such low-ε_{Nd} source could not result in the obvious increase of $\varepsilon_{Nd}(t)$ in the quartz monzonite. The Sr-Nd isotopic compositions of the Paleozoic sedimentary rocks were rarely reported. Nonetheless, because the terrestrial sediments were mainly derived from the erosion of the basement rocks, it is inferred that the shales and sandstones have similar Sr-Nd isotopic compositions to those of the TTG gneisses and thus they could not be the major components responsible for the crustal assimilation. Two representative samples collected from the Ordovician carbonates in the Luxi Block show the $^{87}Sr/^{86}Sr$ of 0.70944–0.70946 and ε_{Nd} of −12 to −9 (recalculated back to 125 Ma) (J.M. Liu et al., 2004), the Nd isotopic compositions of which are much higher than those of the TTG gneisses. These rocks thus might be appropriate for the crustal assimilation, as confirmed by the magma mixing modelling (Fig. 10). Actually, the significant increase of Th concentrations coupled with increasing $\varepsilon_{Nd}(t)$ in the quartz monzonite also supports such assimilation (Fig. 13b), since the Ordovician carbonates not only have high $\varepsilon_{Nd}(t)$ values but also are enriched in Th concentrations (high up to 16 ppm, average > 4 ppm, Liu and Wang, 1996), distinct from the low $\varepsilon_{Nd}(t)$ and low Th features (commonly <4 ppm, Polat et al., 2006; Wang et al., 2009) of the TTG gneisses. Based on the above results, two steps of crustal involvement probably occurred in the Zibo high-Mg diorites (Fig. 14). Firstly, mafic melts derived from the SCLM assimilated ancient middle to upper crustal materials more or less during ascent (step 1), generating the least

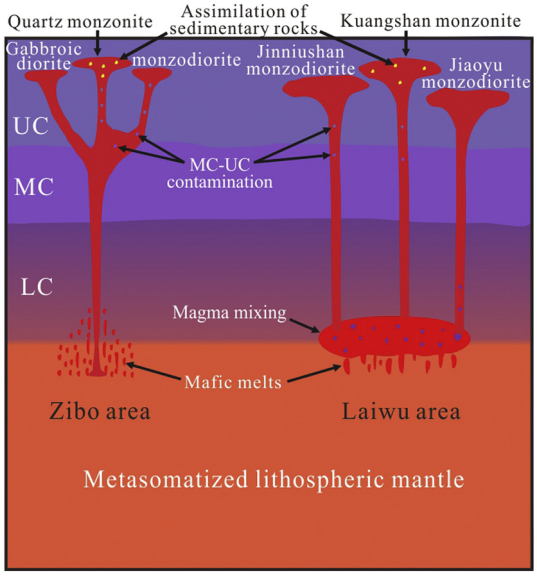

Fig. 14. Genetic model for the generation of Zibo and Laiwu high-Mg diorites. The structures of the NCC crusts refer to Gao et al. (1998).

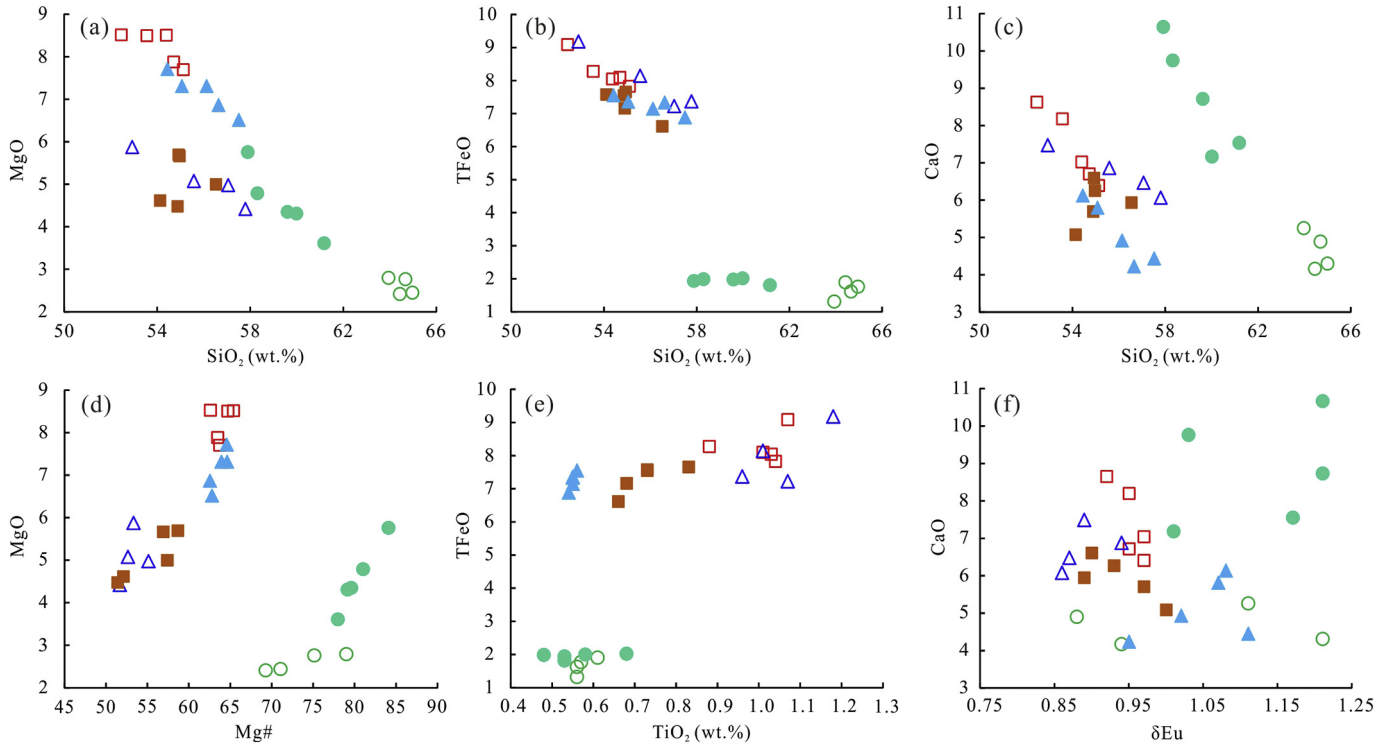

Fig. 15. Plots of MgO vs.SiO_2 (a), TFeO vs. SiO_2 (b), CaO vs. SiO_2 (c), MgO vs. Mg# (d), TFeO vs. TiO_2 (e) and CaO vs. δEu (f) for the Zibo and Laiwu high-Mg diorites. Symbols as in Fig. 9.

contaminated gabbroic diorite and the more contaminated monzodiorite. Secondly, the above melts stored at somewhere of the upper crust and assimilated the Paleozoic sedimentary materials (step 2), especially the carbonates, giving rise to the quartz monzonite (Fig. 14). Considering the quartz monzonite was highly mineralized, the assimilation of sedimentary rocks probably played an important role for the Fe mineralization.

Compared with the Zibo rocks, the Laiwu high-Mg diorites have much lower $\varepsilon_{Nd}(t)$ values (Fig. 10), indicating that more crustal materials should have participated in these rocks. Lower crust seems to be the dominant component responsible for the crustal involvement, as shown by the modelling suggesting that >40% upper crustal materials would be required to generate the isotopic compositions of the Laiwu intrusions (Fig. 10), the amounts of which are unreasonably high for high-Mg dioritic melts. Alternatively, just ~30% lower crustal materials are needed for the least contaminated Jiaoyu monzodiorite. These amounts of lower crustal materials are corroborated by Os isotopic compositions. Chen et al. (2013) used Os isotopic compositions to model the generation of high-Mg diorites in the Zibo and Laiwu areas, concluding that 9%–40% lower crust-derived felsic melts were involved into the SCLM-derived basaltic melts, especially for the rocks with intermediate compositions. Lower crustal involvement can occur in the mantle source through lower crust delamination (e.g., Xu et al., 2008; D.B. Yang et al., 2012), or in the magma chamber through magma mixing (e.g., Chen et al., 2013). Because the Laiwu intrusions are located closely to the Zibo intrusions (<80 km), it is inferred that they shared the same/similar mantle source. If it is true, then the lower crust delamination can be precluded, because it is highly impossible that the delamination just occurred in the Zibo area but not in the Laiwu area within such a close distance. Considering all the Laiwu intrusions have similar $\varepsilon_{Nd}(t)$ values (Fig. 10), the lower crustal materials might be generally homogenized in the magma chamber. It has been suggested that a homogeneous magma chamber can be generated through MASH processes (melting, assimilation, storage and homogenization, Hildreth and Moorbath, 1988), in which underplated mafic magma mixing with crust-derived melts at the lower crust is invoked (Hildreth and Moorbath, 1988; Richards, 2003). However, the sole involvement of lower crust cannot explain the obvious increase of $(^{87}Sr/^{86}Sr)_i$ in the Jinniushan and Kuangshan intrusions. Because the $(^{87}Sr/^{86}Sr)_i$ shows a strong trend to the middle-upper crust (Fig. 10), some middle-upper crustal materials might have also been assimilated, especially in the more felsic Kuangshan monzonite. The Kuangshan monzonite has higher $\varepsilon_{Nd}(t)$ than the more mafic Jiaoyu monzodiorite (Fig. 10), and its $\varepsilon_{Nd}(t)$ increases with decreasing MgO and increasing Th (Fig. 13c and d). These features are almost the same as in the Zibo quartz monzonite, implying that carbonates might have also been assimilated in the Kuangshan monzonite. The assimilation is evidenced by the much higher CaO contents (7.2–10.7 wt%) and CaO/SiO_2 ratios (0.12–0.18) in the Kuangshan intrusion than in the more mafic Jiaoyu and Jinniushan intrusions ($CaO = 4.2–6.1$ wt%, $CaO/SiO_2 = 0.07–0.12$) (Table 1 and Fig. 15c). As a result, two steps of crustal involvement probably also occurred in the Laiwu high-Mg diorites (Fig. 14). Firstly, lower crustal materials were involved into the mantle-derived mafic melts through magma mixing or MASH processes in the magma chamber at the lower crust (step 1), producing the nearly homogeneous parental magmas of the Laiwu intrusions. The parental magmas were contaminated by middle-upper crustal materials more or less during ascent (step 2), generating the Jiaoyu, Jinniushan and Kuangshan intrusions, respectively. Typically, carbonates were assimilated into the Kuangshan intrusion. The Jiaoyu intrusion was least contaminated by the middle-upper crustal materials but might experience more fractional crystallization than the Jinniushan intrusion (Figs. 10 and 13c).

Based on the above results, the assimilation of sedimentary rocks (mainly carbonates) seems to be crucial for the generation of the ore-forming intrusions. It has been observed that in skarn environments stoping of carbonate rocks and related decarbonation reactions can greatly elevate the CO_2 contents of silicate melts (Meinert et al., 2005). In addition, the presence of CO_2 in melts can strongly promote H_2O to be partitioned into fluids (Holloway, 1976). The assimilation of carbonates in this study thus might have contributed to generate the ore-forming fluids.

Table 2
EPMA major element data (wt%) of amphibole from the Zibo and Laiwu high-Mg diorites.

Sample	Spot	SiO_2	Al_2O_3	TiO_2	FeO	MnO	MgO	CaO	Na_2O	K_2O	SrO	F	Cl	Total	Species	T (°C)	P (MPa)	H_2O_{melt} (wt%)
Zibo gabbroic diorite																		
13ZB01	2	50.9	4.86	1.44	9.25	0.19	17.5	11.1	1.25	0.45	0.21	–	–	97.1	Magnesio-ferri-hornblende	756	61.8	3.07
	6	51.5	4.36	1.14	9.38	0.20	17.6	11.4	1.09	0.37	0.12	–	–	97.2	Magnesio-ferri-hornblende	742	54.8	3.23
	9	52.9	4.11	1.02	8.96	0.26	17.4	11.0	0.99	0.36	0.20	–	–	97.3	Magnesio-hornblende	727	51.3	3.58
13ZB05	5	50.4	4.00	0.82	11.7	0.21	16.6	11.5	1.27	0.41	–	0.46	0.03	97.4	Actinolite	768	50.8	3.17
13ZB14	2	51.1	5.30	1.39	9.66	0.22	16.8	11.3	1.22	0.42	0.19	–	–	97.7	Magnesio-ferri-hornblende	757	68.5	3.87
	13	49.7	5.45	1.28	10.8	0.18	16.6	11.1	1.31	0.45	0.21	–	–	97.1	magnesio-ferri-hornblende	770	71.8	3.44
	14	51.1	4.73	1.35	10.4	0.17	17.0	11.1	1.08	0.46	0.16	–	–	97.5	Magnesio-ferri-hornblende	750	59.7	3.20
Zibo quartz monzonite																		
13ZB51	3	53.5	3.51	1.04	8.85	0.30	17.5	11.5	1.28	0.37	0.15	0.31	–	98.2	Actinolite	712	44.2	2.94
	60	52.2	3.50	0.71	9.29	0.30	17.1	12.1	1.80	0.35	–	0.43	0.02	97.7	Actinolite	734	45.1	2.65
	62	53.4	3.19	0.49	6.96	0.07	19.1	12.5	1.36	0.31	–	0.55	0.05	97.9	Actinolite	730	41.3	2.49
	65	51.7	3.97	1.03	9.47	0.31	16.7	11.7	1.75	0.36	–	0.41	0.00	97.4	Actinolite	737	50.6	2.97
13ZB55	1	51.7	3.19	0.64	10.4	0.41	18.0	12.0	1.25	0.31	–	–	0.12	97.9	Actinolite	784	41.7	2.55
	4	52.0	3.71	0.62	10.2	0.49	18.0	11.3	1.43	0.40	–	–	0.02	98.2	Actinolite	791	47.2	2.44
Laiwu Kuangshan monzonite																		
13LW05	1	51.4	4.42	1.00	9.44	0.22	17.9	11.3	1.26	0.36	0.17	0.46	–	97.8	Magnesio-ferri-hornblende	750	55.4	3.01
	5	51.2	4.57	1.03	9.75	0.29	17.7	11.2	1.11	0.39	0.14	0.43	–	97.8	Magnesio-ferri-hornblende	750	57.3	3.21
	8	50.9	5.01	1.26	9.80	0.20	17.3	11.0	1.48	0.41	0.12	0.56	–	98.0	Magnesio-ferri-hornblende	757	63.9	3.12
	13	51.1	5.15	1.25	9.34	0.27	17.5	11.2	1.52	0.41	0.12	0.55	–	98.3	Magnesio-ferri-hornblende	763	65.8	3.18
Laiwu Jiaoyu monzodiorite																		
13LW15	7	49.4	5.56	1.03	13.9	0.36	15.0	10.8	1.48	0.48	0.08	0.24	–	98.4	Magnesio-ferri-hornblende	761	73.7	3.77
	10	51.2	4.43	1.00	13.0	0.45	15.3	10.8	1.02	0.39	0.12	–	–	97.7	Magnesio-ferri-hornblende	730	56.0	3.86
	12	50.4	4.66	0.79	13.7	0.48	14.9	10.5	1.23	0.36	0.21	–	–	97.3	Magnesio-ferri-hornblende	729	59.7	3.94
	14	50.6	4.51	0.71	13.3	0.39	14.9	11.0	1.26	0.38	0.19	0.17	–	97.3	Magnesio-ferri-hornblende	722	57.9	4.01
13LW16	304	51.4	4.09	1.12	14.0	0.44	14.0	11.3	1.16	0.48	–	–	0.06	98.1	Magnesio-ferri-hornblende	707	52.2	4.04
	318	51.2	4.08	0.89	13.7	0.39	14.6	11.3	1.22	0.48	–	–	0.07	97.9	Magnesio-ferri-hornblende	713	52.0	3.69
	329	51.3	4.05	1.08	13.7	0.36	14.1	11.4	1.34	0.50	–	–	0.08	97.9	Actinolite	711	52.0	3.80
	334	50.1	4.92	1.29	14.0	0.34	14.1	11.4	1.58	0.59	–	–	0.08	98.4	Magnesio-ferri-hornblende	744	64.1	3.51
Laiwu Jinniushan monzodiorite																		
13LW57	209	47.2	8.23	0.68	13.1	0.23	15.4	10.8	1.82	0.43	–	–	–	97.9	Magnesio-ferri-hornblende	828	139	4.85
	215	48.5	6.83	0.60	12.2	0.24	15.3	11.8	1.81	0.42	0.04	0.12	0.00	97.8	Pargasite	805	102	4.48
	220	47.3	7.29	0.52	12.7	0.00	16.2	11.7	1.73	0.33	–	–	0.00	97.8	Magnesio-ferri-hornblende	835	112	4.30
	226	48.0	6.80	1.12	12.2	0.27	15.3	12.0	1.72	0.51	0.03	0.16	–	98.0	Magnesio-hastingsite	816	101	4.03
	235	46.8	7.77	1.43	11.8	0.17	14.9	11.4	2.23	0.57	0.05	–	–	97.2	Pargasite	842	131	3.99
	237	48.9	6.40	0.64	12.1	0.23	15.8	11.5	1.77	0.50	0.05	–	–	97.8	Magnesio-ferri-hornblende	794	90.8	3.79
	240	49.8	6.84	0.66	10.8	0.28	15.9	10.9	1.58	0.44	0.16	–	–	97.4	Magnesio-ferri-hornblende	780	100	4.88

The nomenclature of amphibole is based on the International Mineralogical Association (IMA) classification (Hawthorne et al., 2012) and calculated using an excel spreadsheet from Locock (2014). The T, P and H_2O contents are calculated using the method of Ridolfi et al. (2010). "–" indicates that the concentration is lower than the detection limit.

5.2. The role of fractional crystallization

As mentioned before, both the Zibo and Laiwu high-Mg diorites show wide variations in major elements (Table 1 and Fig. 15), which can be partly explained by the crustal involvement. However, since fractional crystallization is one of the most common magmatic processes in mafic to felsic evolution of genetically associated magmas, the variations might have also been affected by the fractional crystallization. From mafic to more felsic high-Mg diorites in this study, the major elements commonly show poor correlations or do not show well correlated relationships that can be reasonably explained by fractional crystallization (Fig. 15). This implies that the more felsic high-Mg diorites, especially the most felsic strongly mineralized rocks, could not be evolved from the mafic high-Mg diorites through continuous fractional crystallization. Crustal involvement seems to play more important role for generating different types of high-Mg diorites. Nonetheless, within an individual rock, fractional crystallization likely played a role. The MgO, TFeO and CaO within an individual rock commonly show well-correlated negative relationships with SiO_2 (Fig. 15a–c), combined with other covariant diagrams such as MgO vs. Mg#, TFeO vs. TiO_2 and CaO vs. δEu (Fig. 15d–f), suggesting that fractional crystallization of mafic minerals such as pyroxene, amphibole, plagioclase and Fe-Ti oxides occurred in most of the rocks.

Notably, in both the Zibo and Laiwu high-Mg diorites, the Mg# values decrease steadily from the most mafic ore-barren rocks to the less mafic rocks, but increase drastically to the most felsic strongly mineralized rocks (Fig. 15d). The drastic increase of Mg# values cannot be resulted from crustal contamination, because both the lower and upper crusts in the study region have much lower Mg# values (<50, Gao et al., 1998). In a normal fractional crystallization process, the Mg# values commonly decrease due to the fractionation of mafic minerals which more quickly scavenges Mg from the magmas, as indicated by the positive correlation between MgO and Mg# within an individual rock (Fig. 15d). It is noted that the high Mg# feature of the strongly mineralized rocks is mainly due to the drastic decrease of TFeO with steady decrease of MgO (Fig. 15a, b, d). This indicates that an efficient extraction of Fe from the ore-forming magmas occurred. Fractional crystallization of Fe-oxide minerals (such as magnetite and ilmenite) is effective in removing Fe from the magmas (Toplis and Carroll, 1995). However, large-scale fractional crystallization of Fe-oxide minerals is not supported by the petrographic evidence showing minor Fe-oxide minerals (magnetite ± ilmenite) in both the mafic and felsic intrusions. In addition, the whole-rock TFeO contents remain stable with increasing SiO_2 within the strongly mineralized rocks (Fig. 15b), clearly precluding the significant fractional crystallization of Fe-oxide minerals. Therefore, a process beyond fractional crystallization might have occurred. Experimental studies showed that chloride liquid is one of the most important Fe-carriers at the magmatic-hydrothermal conditions (commonly complexed as $FeCl_2$, Whitney et al., 1985; Simon et al., 2004; Bell and Simon, 2011), which can effectively transport Fe from the magmas into the

Table 3
Whole-rock Sr-Nd-Pb isotopic compositions of the Zibo and Laiwu high-Mg diorites.

Sample	Age (Ma)	Rb (ppm)	Sr (ppm)	$^{87}Rb/^{86}Sr$	$^{87}Sr/^{86}Sr$	(2σ)	$(^{87}Sr/^{86}Sr)_i$	Sm (ppm)	Nd (ppm)	$^{147}Sm/^{144}Nd$	$^{143}Nd/^{144}Nd$	(2σ)	$(^{143}Nd/^{144}Nd)_i$	$\varepsilon_{Nd}(t)$	T_{DM} (Ma)	$(^{208}Pb/^{204}Pb)_i$	$(^{207}Pb/^{204}Pb)_i$	$(^{206}Pb/^{204}Pb)_i$
Zibo gabbroic diorite																		
13ZB01	131.6	45.5	679	0.1938	0.705169	0.000007	0.704807	5.81	28.0	0.1254	0.512247	0.000002	0.512139	−6.4	1559	37.1148	15.3526	17.1427
13ZB05	131.6	41.3	670	0.1783	0.705060	0.000008	0.704726	6.44	30.1	0.1293	0.512297	0.000005	0.512186	−5.5	1541	37.0874	15.3481	17.1101
13ZB07	131.6	39.0	704	0.1605	0.705175	0.000013	0.704875	5.97	29.1	0.1241	0.512250	0.000007	0.512144	−6.3	1530			
13ZB14	131.6	34.3	694	0.1429	0.704999	0.000011	0.704732	5.49	25.7	0.1294	0.512203	0.000007	0.512305	−5.4	1529			
Zibo monzodiorite																		
16ZB16	131.3	69.7	564	0.3575	0.706642	0.000007	0.705974	5.43	26.5	0.1239	0.512087	0.000003	0.511980	−9.5	1803	37.3173	15.3672	17.1232
16ZB29	131.3	63.8	676	0.2730	0.706462	0.000008	0.705952	5.94	27.7	0.1296	0.512137	0.000005	0.512026	−8.6	1835	37.6734	15.4439	17.5855
16ZB30	131.3	64.6	703	0.2658	0.706262	0.000007	0.705761	6.64	31.8	0.1391	0.512125	0.000005	0.512005	−9.0	2092	37.7537	15.4416	17.6291
Zibo quartz monzonite																		
13ZB48	129.7	64.1	647	0.2865	0.706586	0.000012	0.706058	4.12	24.0	0.1039	0.512163	0.000006	0.512075	−7.7	1371			
13ZB51	129.7	44.0	604	0.2107	0.706081	0.000007	0.705692	5.75	33.5	0.1038	0.512139	0.000003	0.512051	−8.2	1402	37.3636	15.4041	17.4104
13ZB55	129.7	89.6	524	0.4945	0.706831	0.000009	0.705919	4.02	21.4	0.1138	0.512161	0.000011	0.512064	−7.9	1510	37.0594	15.4466	17.3078
13ZB56	129.7	81.7	665	0.3552	0.706240	0.000009	0.705585	3.70	20.5	0.1092	0.512143	0.000012	0.512051	−8.2	1468			
Laiwu Kuangshan monzonite																		
13LW03	129.3	15.4	689	0.0645	0.707625	0.000010	0.707507	34.3	175	0.1189	0.511761	0.000012	0.511661	−15.8	2228	37.1146	15.3265	16.8834
13LW04	129.3	27.5	748	0.1064	0.707418	0.000007	0.707223	3.69	20.7	0.1077	0.511774	0.000002	0.511683	−15.4	1976	37.1927	15.3469	16.9861
13LW07	129.3	50.5	593	0.2467	0.707906	0.000011	0.707452	3.53	16.8	0.1270	0.511819	0.000013	0.511711	−14.8	2334			
13LW09	129.3	25.2	790	0.0923	0.707588	0.000007	0.707418	4.70	28.9	0.0983	0.511757	0.000002	0.511674	−15.6	1838	37.1695	15.3463	16.9619
Laiwu Jiaoyu monzodiorite																		
13LW10	131.0	45.0	686	0.1898	0.707178	0.000008	0.706824	5.04	25.8	0.1181	0.511750	0.000003	0.511649	−16.0	2226	36.5266	15.2590	16.6090
13LW15	131.0	41.8	583	0.2073	0.706721	0.000013	0.706334	5.46	27.0	0.1227	0.511782	0.000010	0.511677	−15.5	2286			
13LW16	131.0	39.4	638	0.1787	0.706621	0.000007	0.706288	4.36	22.5	0.1171	0.511758	0.000002	0.511657	−15.8	2193	36.3061	15.2045	16.3342
13LW17	131.0	49.6	568	0.2528	0.706730	0.000010	0.706259	4.40	23.6	0.1130	0.511749	0.000011	0.511652	−16.0	2117			
Laiwu Jinniushan monzodiorite																		
13LW54	130.1	33.7	228	0.4277	0.708128	0.000008	0.707338	3.27	16.0	0.1235	0.511795	0.000003	0.511690	−15.2	2284	37.5290	15.4181	17.5168
13LW55	130.1	40.9	380	0.3114	0.707569	0.000010	0.706994	3.04	14.4	0.1276	0.511813	0.000012	0.511704	−15.0	2362			
13LW56	130.1	33.0	325	0.2938	0.707668	0.000007	0.707125	3.16	15.3	0.1248	0.511802	0.000003	0.511696	−15.1	2306	37.1950	15.4054	17.5966
13LW57	130.1	34.5	405	0.2466	0.707514	0.000012	0.707058	3.40	16.7	0.1232	0.511817	0.000010	0.511712	−14.8	2239			
13LW58	130.1	30.0	346	0.2510	0.707519	0.000010	0.707055	3.58	18.1	0.1199	0.511801	0.000011	0.511699	−15.1	2188			

Chondrite Uniform Reservoir (CHUR) values ($^{87}Rb/^{86}Sr = 0.0847$, $^{87}Sr/^{86}Sr = 0.7045$, $^{147}Sm/^{144}Nd = 0.1967$, $^{143}Nd/^{144}Nd = 0.512638$) are used for the calculation. $\lambda_{Rb} = 1.42 \times 10^{-11}$ year^{-1}, $\lambda_{Sm} = 6.54 \times 10^{-12}$ year^{-1} (Lugmair and Harti, 1978).

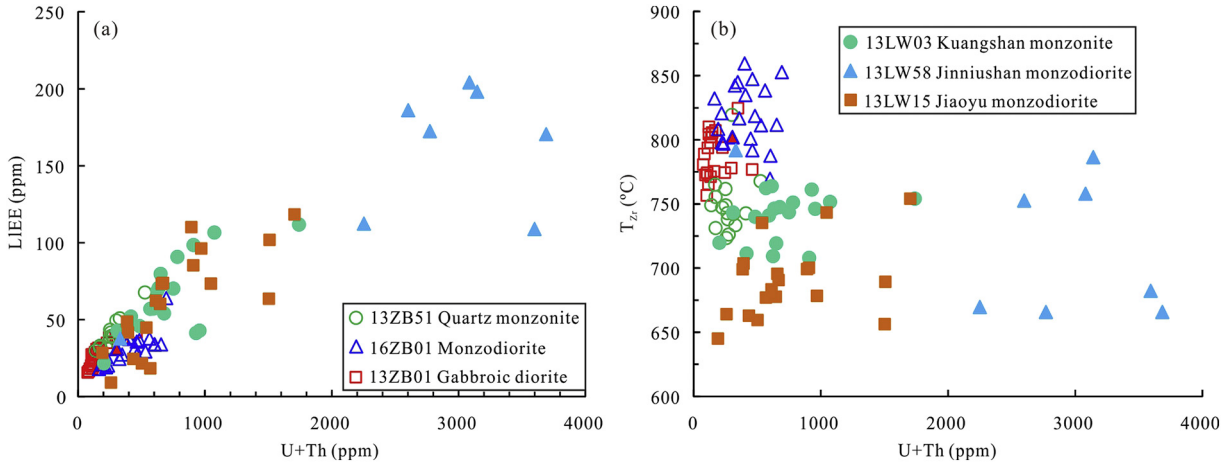

Fig. 16. Plots of LREE vs. U + Th (a) and T_{Zr} vs. U + Th (b) for zircons from the Zibo and Laiwu high-Mg diorites.

magmatic-hydrothermal fluids (Simon et al., 2004; Bell and Simon, 2011). Because more felsic magmas have much lower solubilities of Cl and H_2O (Webster, 2004), the strongly mineralized rocks in this study might have suffered significant exsolution of hydrosaline liquids, which scavenged Fe from the melts and thus elevated the Mg# values of the residual magmas. This process was probably enhanced by the assimilation of carbonates, since carbonates have remarkable effect on promoting H_2O to be partitioned into fluids (Holloway, 1976; Meinert et al., 2005). The lowest H_2O contents in the strongly mineralized rocks confirm the above fluid exsolution, as discussed below.

5.3. The physicochemical conditions

Physicochemical conditions, such as water content (H_2O), temperature (T), pressure (P) and oxygen fugacity (*f*O2), commonly play a significant role in whether a magma can generate mineralization or not (Richards, 2011, 2013). Ridolfi et al. (2010) proposed a powerful method which uses the compositions of amphibole to calculate the H_2O_{melt}, T and P conditions of calc-alkaline rocks. The high-Mg diorites in this study are mainly calc-alkaline and most of them contain abundant amphiboles (except the Zibo monzodiorite), suitable for applying this method. The calculated results show that in the Zibo area the H_2O contents decrease from the most mafic ore-barren gabbroic diorite (3.1–3.9 wt% H_2O) to the most felsic strongly mineralized quartz monzonite (2.4–3.0 wt% H_2O), while in the Laiwu area such trend occurs from the mafic ore-barren Jinniushan (3.8–4.9 wt% H_2O) and Jiaoyu monzodiorites (3.5–4.0 wt% H_2O) to the more felsic strongly mineralized Kuangshan monzonite (3.0–3.2 wt% H_2O) (Table 2). The Laiwu intrusions have higher H_2O contents than those of the Zibo intrusions. In addition, both the strongly mineralized rocks have the lowest H_2O contents. This trend is also confirmed by the whole-rock loss on ignition (LOI), which shows that in the Zibo area the quartz monzonite (0.66–0.94, averaging at 0.77) has lower LOI than those of the gabbroic diorite (0.72–0.94 averaging at 0.85) and the monzodiorite (0.64–1.18, averaging at 0.99) while in the Laiwu area the LOI is much lower in the Kuangshan monzonite (0.86–1.56, averaging at 1.14) than in the Jinniushan (1.84–2.96, averaging at 2.20) and Jiaoyu (1.36–1.88, averaging at 1.54) monzodiorites (Table 1). Because the LOI can roughly represent the volatiles in the rocks, the above trend suggests less volatiles being available in the strongly mineralized intrusions. This is meaningful because it likely indicates efficient fluid exsolution from the magmas that subsequently contributed to generate the ore-forming fluids. High H_2O contents in the parental magmas seem to be favorable for Fe mineralization, as supported by the much larger scale Fe mineralization induced by the more hydrous Laiwu intrusions.

Ti-in-zircon thermometer (T_{Zr}) is a simple and robust thermometer which has been widely applied to estimate the temperatures of igneous and metamorphic rocks in recent years (e.g., Watson et al., 2006; Baldwin et al., 2007; Ferry and Watson, 2007; Fu et al., 2008). By using the revised Ti-in-zircon thermometer ($\log Ti_{zircon}(ppm) = 5.711 - 4800 / T_{Zr}(K) - \log\alpha_{SiO_2} + \log\alpha_{TiO_2}$) (Ferry and Watson, 2007), the calculated T_{Zr} temperatures in the Zibo gabbro diorite, monzodiorite and quartz monzonite are 788 ± 18 °C, 818 ± 24 °C and 744 ± 13 °C, respectively, whereas in the Laiwu Jinniushan, Jiaoyu and Kuangshan intrusions are 721 ± 56 °C, 690 ± 29 °C and 740 ± 18 °C (Supplementary Table S2), respectively. The temperatures are lower in the Laiwu intrusions than in the Zibo intrusions, and no systematic trend occurs from the mafic to the more felsic intrusions. This seems to contradict the common observation that mafic rocks have higher T_{Zr} than those of the felsic rocks (Valley et al., 2006; Fu et al., 2008). Actually, in addition to the TiO_2 and SiO_2 activities of the melts, other factors such as pressure, subsolidus resetting of Ti compositions, non-Henry's Law substitution of Ti in zircon, disequilibrium crystallization from melts and growth of zircons in late melts with evolved hydrous composition, may also affect the apparent temperature of the Ti-in-zircon thermometer (Fu et al., 2008; Claiborne et al., 2010). It is noted that the remarkably low and widely varied T_{Zr} temperatures in the Laiwu Jinniushan and Jiaoyu monzodiorites are accompanied by the highest H_2O contents, indicating that the Ti contents in zircon grains might be disturbed by the hydrous conditions. This can be supported by the zircon geochemistry. In the Zibo and Laiwu zircons, the U + Th and LREE concentrations are positively correlated and are much more enriched in the Laiwu zircons (Fig. 16a). In addition, the U + Th concentrations increase drastically as the T_{Zr} decreases to be low (<750 °C) (Fig. 16b). This phenomenon has been identified in other igneous rocks worldwide, such as in the Spirit Mountain batholith, Nevada (Claiborne et al., 2006, 2010). In the Spirit Mountain batholith, the U, Th and LREE concentrations in zircons increase sharply while the T_{Zr} falls to approximately 725 °C. It was interpreted to be a consequence of increased rate of crystallization for a given decrease in T as the system approaches eutectic-like conditions. Other studies also proved that zircon grains crystallized from hydrous melts can give much lower T_{Zr} comparable to the solidus temperatures (Harrison et al., 2007; Fu et al., 2008). The drastic increase of U, Th and LREEs in this study begins at about 750 °C (Fig. 16b), higher than that of the Spirit Mountain batholith. Because the high-Mg diorites are more mafic than the Spirit Mountain batholith, the eutectic-like conditions might be achieved at higher temperatures (~750 °C). The widely varied T_{Zr} in the high-Mg diorites well confirms the hydrous features of the host magmas, but it seems to be not a good thermometer for the hydrous conditions.

To further constrain the P-T conditions, other thermobarometer needs to be invoked. Also using the compositions of amphibole, based on the method of Ridolfi et al. (2010), the T and P conditions of the high-Mg diorites are calculated. The results show that the Zibo gabbroic diorite and quartz monzonite are characterized by 753 ± 15 °C and 748 ± 32 °C, respectively. For the Laiwu intrusions, the temperatures are 814 ± 22 °C, 727 ± 18 °C and 755 ± 6 °C in the Jinniushan, Jiaoyu and Kuangshan intrusions, respectively (Table 2). These temperatures are broadly consistent with those obtained from the Ti-in-zircon thermometer, but more concentrated at ~750 °C. Except for the Jinniushan monzodiorite, the other rocks show similar temperatures. No systematic difference occurs between the ore-barren and ore-bearing intrusions. For the crystallization pressure, also except for the Jinniushan monzodiorite (91–139 MPa), the other rocks have similar pressures (41–74 MPa) (Table 2). All the pressures are quite low, indicating that the high-Mg diorites were probably emplaced at very shallow crustal levels. The wide involvement of upper crustal materials confirms the shallow emplacement. Actually, the shallow emplacement is also supported by the extreme crustal extension of the eastern NCC during the early Cretaceous (e.g., Wu et al., 2005; Mao et al., 2011; Li et al., 2015; Pirajno and Zhou, 2015), which has been considered to be induced by the remarkable upwelling of the asthenosphere (Chen et al., 2006; Tang et al., 2013). Because the ore-barren and ore-bearing intrusions do not show systematic difference in P-T conditions, the Fe mineralization might not be significantly controlled by the P-T factors.

All the high-Mg diorites have accessory mineral of magnetite, similar to the oxidized granitoids (Takagi and Tsukimura, 1997). Based on the redox classification scheme of Blevin (2004), the high Fe_2O_3/FeO ratios of these rocks indicate that they are moderately to strongly oxidized (Fig. 17a), consistent with the features of plutons associated with Fe skarn deposits worldwide (Fig. 17b). It seems that the strongly mineralized intrusions are less oxidized than the ore-barren intrusions (Fig. 17a). Because oxide mineralogy and partitioning data among mineral phases can provide a more detailed assessment of magma oxidation state than do by whole-rock chemical analyses (Frost, 1991; Meinert et al., 2005), we use the elements sensitive to oxygen fugacity, such as V and Ti in magnetite, to further constrain the oxidation states of the host magmas. Vanadium has a range of possible oxidation states (such as V^{3+}, V^{4+}, V^{5+}, Toplis and Corgne, 2002; Bordage et al., 2011), the partitioning of which between magnetite and melt strongly depends on oxygen fugacity, and also on melt alumina saturation index (ASI) as well as temperature (T) to some extent (Arató and Audétat, 2017). According to the method of Arató and Audétat (2017) ($\log D_V^{mgt/melt} = 0.3726 \times 10{,}000/T(K) + 2.0465 \times ASI - 0.4773 \times \Delta FMQ - 2.1214$), the calculated ΔFMQ in the Zibo high-Mg diorites increases slightly from the most mafic ore-barren gabbroic diorite (2.91–3.33, averaging at 3.14) to the less mafic moderately mineralized monzodiorite (3.24–3.41, averaging at 3.35), but decreases obviously to the most felsic strongly mineralized quartz monzonite (2.70–3.0, averaging at 2.86). For the Laiwu high-Mg diorites, the ΔFMQ also increases from the most mafic ore-barren Jinniushan monzodiorite (2.86–3.21, averaging at 3.02) to the less mafic ore-barren Jiaoyu monzodiorite (3.68–3.96, averaging at 3.87), but decreases drastically to the most felsic strongly mineralized Kuangshan monzonite (2.56–3.11, averaging at 2.77). Both the strongly mineralized intrusions have the lowest ΔFMQ, indicating that they are less oxidized. This is confirmed by the Ti contents in magnetite. Experiments have shown that Ti in magmatic magnetite is mainly controlled by oxygen fugacity and temperature, the contents of which commonly become lower at higher oxygen fugacities or lower temperatures due to the exsolution of ilmenite$_{SS}$ (hematite-ilmenite solid solution, Fe_2O_3-$FeTiO_3$) or Ti partitioning into silicate minerals (e.g., Buddington and Lindsley, 1964; Spencer and Lindsley, 1981; Toplis and Carroll, 1995; Lattard et al., 2005). In the Zibo high-Mg diorites, the Ti contents (wt% TiO_2) of magnetite decrease slightly from the gabbroic diorite (0.16–0.77, averaging at 0.34) to the monzodiorite (0.14–0.34, averaging at 0.20), but increase drastically to the quartz monzonite (19.8–29.0, averaging at 23.8). In the Laiwu intrusions, the Ti contents decrease from the Jinniushan monzodiorite (0.08–1.72, averaging at 0.99) to the Jiaoyu monzodiorite (0.10–1.64, averaging at 0.47), but increase obviously to the Kuangshan monzonite (3.08–5.76, averaging at 4.49) (Supplementary Table S4). Both the strongly mineralized intrusions have the highest Ti contents in magnetite. Based on the phase diagram of *f*O2-T-X for the magnetite-ulvöspinel$_{SS}$ (Fe_3O_4-Fe_2TiO_4 solid solution) and coexisting hematite-ilmenite$_{SS}$ (Fe_2O_3-$FeTiO_3$ solid solution) (Buddington and Lindsley, 1964; Spencer and Lindsley, 1981), in combination with the crystallization temperatures of the host magmas (727–814 °C), the strongly mineralized intrusions are clearly characterized by lower oxygen fugacities. Because magnetite will crystallize early in the magma if the oxygen fugacity is very high (Toplis and Carroll, 1995), the ore-forming magmas in this study might benefit from the lower oxygen fugacities due to the magnetite crystallization being suppressed in the early magmas, facilitating the Fe to be scavenged by the late exsolving magmatic-hydrothermal fluids.

5.4. Implications for Fe mineralization

Meinert (1995) summarized the major and trace elements data for plutons related to Fe, Au, Cu, Zn, W, Mo, and Sn skarn deposits, concluding that plutons associated with Fe and Au skarns are more mafic, Au and Sn skarn plutons are more reduced, and Cu, Zn and Mo skarn

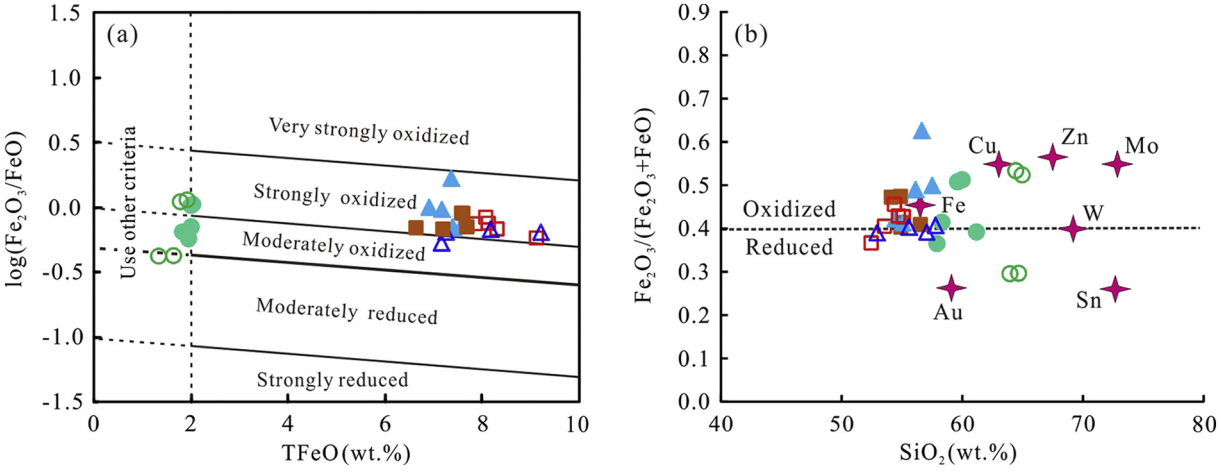

Fig. 17. Plots of log (Fe_2O_3/FeO) vs. TFeO (a) and Fe_2O_3/(Fe_2O_3 + FeO) vs. SiO_2 (b) for the Zibo and Laiwu high-Mg diorites. (a) and (b) are from Blevin (2004) and Meinert et al. (2005), respectively. In (a), the boundary between the moderately reduced and moderately oxidized fields approximates the FMQ buffer curve (Blevin, 2004). In (b), the average values of Fe, Cu, Zn, Mo, Au, W and Sn skarn plutons are also shown (Meinert et al., 2005). Symbols as in Fig. 9.

plutons are more oxidized than average skarn plutons. The high-Mg diorites in this study are mafic to intermediate with derivation mainly from the lithospheric mantle, showing major elements close to the plutons related to Fe skarns worldwide (Fig. 17b). This indicates that magma composition rather than tectonic setting is more crucial for the Fe mineralization. It can be easily understood that mantle-derived mafic melts are more enriched in Fe, which basically facilitate to provide ore-forming metals.

Although mantle components seem to be indispensable for the Fe mineralization, it is noted that numerous mantle-derived high-Mg diorites were generated at the eastern NCC, but only some of them formed economic Fe mineralization. This implies that other factors beyond mantle components should have also worked. Paleozoic sedimentary rocks were typically assimilated into the strongly mineralized intrusions in this study, which seem to contribute a lot to the Fe mineralization. The Paleozoic sedimentary rocks are composed mainly of carbonates with some interbedded shales, sandstones and evaporitic rocks. The involvement of carbonates, which can significantly increase the CO_2 contents of the melts, might have promoted the H_2O to be partitioned into the fluids (Holloway, 1976; Meinert et al., 2005). This process was favorable for generating ore-forming fluids due to the efficient fluid exsolution, as indicated by the fact that the strongly mineralized intrusions have the lowest H_2O contents. The evaporitic rocks, which are enriched in chlorides, also seem to play a role. It is noted that the strongly mineralized intrusions have the remarkably high Mg# values (69–84), which cannot be explained by factional crystallization or crustal contamination. Alternatively, because Fe is highly complexed and transported by chlorides at magmatic-hydrothermal conditions (mainly as $FeCl_2$, Whitney et al., 1985; Simon et al., 2004; Bell and Simon, 2011), scavenging of Fe by Cl-rich fluids would be the most feasible way to increase the Mg# values in the more felsic magmas. If it is true, the perfect source providing abundant Cl would be the chlorides in the evaporitic rocks. Therefore, the assimilation of evaporitic rocks might have contributed to effectively scavenge Fe from the magmas into the magmatic-hydrothermal fluids. In addition, because Fe will be partitioned into Fe-oxides (e.g., magnetite and hematite) or silicate minerals if the oxygen fugacity of the melts is too high or too low (Toplis and Carroll, 1995), a suitable oxygen fugacity is required to keep the Fe in the melts and subsequently facilitate the Fe to be scavenged by fluids. The strongly mineralized intrusions in both the Zibo and Laiwu areas show lower oxygen fugacities than the more mafic ore-barren intrusions, implying that reduction of the oxidized magmas occurred. The shales interbedded with the carbonates in the study region are commonly coal-bearing or black shales (Wei et al., 2011), assimilation of which would lead to the reduction of the magmas. It is thus inferred that assimilation of shales occurred and contributed to generate the suitable oxygen fugacities in the ore-forming magmas. In conclusion, the involvement of Paleozoic sedimentary rocks created favorable physicochemical conditions for Fe extraction and transportation from the magmas into the fluids, which thus seems to be crucial for the Fe mineralization. Actually, involvement of sedimentary rocks into intrusions contributing to generate Fe skarn deposits has been widely identified in other places, such as in the Handan-Xingtai area of central NCC (e.g., Zhang et al., 2014; Wen et al., 2017) and the Middle-Lower Yangtze River Metallogenic Belt of SCB (e.g., Hou et al., 2010, 2012; Mao et al., 2012). This not only supports the conclusion of this study, but also indicates that upper crustal involvement might always be crucial for generating Fe skarn mineralization.

5.5. Geodynamic significance

HMAs have been commonly considered to occur in arc settings with the derivation mainly from metasomatized mantle wedge or slab melts interacting with mantle peridotite. However, in this study, the high-Mg diorites were co-developed with I- to A-type granites, alkaline rocks, bimodal volcanics, mafic dike swarms, carbonatite dikes, metamorphic core complexes and rift basins (Ren et al., 2002; Wu et al., 2005; Pirajno et al., 2009; Windley et al., 2010; Pirajno and Zhou, 2015), which occurred within an intracontinental extension. This suggests that the HMAs can be produced at various tectonic settings beyond the arc settings. More importantly, since the high-Mg diorites in this study have little relationships with the oceanic slab melts, the classic genetic mechanisms for the HMAs need to be reevaluated. Mafic melts derived from an anciently metasomatized and recently hydrated SCLM interacting with various continental crustal materials is the basic mechanism for the generation of the high-Mg diorites in this study. The formation processes indicate remarkable crust-mantle interactions, including the mantle hydration by deeply subducted oceanic slab and the crustal assimilation by underplating mafic melts. These significant crust-mantle interactions might be attributed to the unique geodynamic regime of the eastern NCC during the Mesozoic. Geophysical investigations have shown that asthenospheric upwelling occurred in the eastern NCC since the late Mesozoic, especially along the Tan-Lu fault (Chen et al., 2006). The upwelling not only led to the extreme extension of the lithosphere, but also promoted the large-scale mafic underplating and the subsequent interaction with various crustal materials. Asthenospheric upwelling can be caused by deep subduction of oceanic slab, as exampled by the upwelling flows in the big mantle wedge above the stagnant Pacific slab in the mantle transition zone beneath the northeastern Asian continent (Xu et al., 2011; Liu et al., 2017; Zhao et al., 2017). It is thus inferred that the Paleo-Pacific Oceanic Plate had also subducted deeply into the transition zone beneath the eastern NCC (Windley et al., 2010), which released great amounts of water into the mantle (Komiya and Maruyama, 2007; Windley et al., 2010), inducing the remarkable upwelling of the asthenosphere. In addition, it has been identified that the Paleo-Pacific Plate abruptly changed its subduction direction during the early Cretaceous (Maruyama et al., 1997; Sun et al., 2007), which could also assist the crustal extension and asthenospheric upwelling (Sun et al., 2007). Therefore, the large-scale asthenospheric upwelling induced by the deep subduction of the Paleo-Pacific Plate into the transition zone is considered as the major geodynamic mechanism responsible for the wide development of high-Mg diorites and the associated mineralizations in the eastern NCC. This geodynamic regime is thus different from those in typical arc settings.

6. Conclusions

Based on the detailed comparisons in geochronology, geochemistry, isotopic compositions and physicochemical conditions between the ore-barren and ore-bearing high-Mg diorites from the Zibo and Laiwu areas in the eastern NCC, the genesis of the high-Mg diorites as well as the crucial factors controlling the Fe mineralization were investigated, leading to the following conclusions:

(1) The high-Mg diorites were emplaced at the early Cretaceous (130–132 Ma), generally coeval with the remarkable lithospheric thinning in the eastern NCC.
(2) The high-Mg diorites were mainly derived from an anciently metasomatized and recently hydrated SCLM, but contaminated by various crustal materials. The Zibo gabbroic diorite was least contaminated and denotes the primitive melts from the SCLM. About 20% middle-upper crustal materials were assimilated into the Zibo monzodiorite and quartz monzonite during magma ascent, whereas at least 30% lower crustal materials were involved into the Laiwu Jiaoyu, Jinniushan and Kuangshan intrusions through magma mixing. Paleozoic sedimentary rocks (e.g., carbonates) were particularly assimilated into the strongly mineralized intrusions.
(3) The strongly mineralized intrusions have the lowest H_2O contents, the highest Mg# values and the lowest $fO2$, which were attributed to the assimilation of sedimentary rocks. The assimilation promoted fluid exsolution and metal extraction from the melts, being crucial for generating ore-forming fluids.

(4) The high-Mg diorites were produced within an intracontinental extension. The crustal extension was mainly resulted from the asthenospheric upwelling, which might be induced by the stagnant Paleo-Pacific Oceanic Plate in the transition zone beneath the eastern NCC.

Acknowledgements

We are grateful to Nengping Shen for help during Sr-Nd-Pb isotopic analyses, to Zhihui Dai for help during LA-ICP-MS analyses, to Wenqin Zheng, Xiang Li and Lei Shu for help during EPMA analyses and to Shaohua Dong for help during SEM analyses. Three anonymous reviewers and Thomas Ulrich are also thanked for their constructive and valuable comments. This study is financially supported by the Natural Science Foundation of China (41472079), the National Key Research and Development Program of China (Grant No. 2016YFC0600105) and the CAS "Light of West China" program.

Appendix A. Supplementary data

Supplementary data to this article can be found online at https://doi.org/10.1016/j.gr.2019.03.008.

References

Aguillo'n-Robles, A., Calmus, T., Benoit, M., Bellon, H., Maury, R.C., Cotton, J., Bourgois, J., Michaud, F., 2001. Late Miocene adakites and Nb-enriched basalts from Vizcaino Peninsula, Mexico: indicators of East Pacific Rise subduction below southern Baja California. Geology 29, 531–534.

Arató, R., Audétat, A., 2017. Experimental calibration of a new oxybarometer for silicic magmas based on vanadium partitioning between magnetite and silicate melt. Geochim. Cosmochim. Acta 209, 284–295.

Baldwin, J.A., Brown, M., Schmitz, M.D., 2007. First application of titanium-in-zircon thermometry to ultrahigh-temperature metamorphism. Geology 35, 295–298.

Ballard, J.R., Palin, J.M., Campbell, I.H., 2002. Relative oxidation states of magmas inferred from Ce(IV)/Ce(III) in zircon: application to porphyry copper deposits of northern Chile. Contrib. Mineral. Petrol. 144, 347–364.

Bell, A.S., Simon, A., 2011. Experimental evidence for the alteration of the Fe3+/ΣFe of silicate melt caused by the degassing of chlorine-bearing aqueous volatiles. Geology 39, 499–502.

Belousova, E., Griffin, W., O'Reilly, S.Y., Fisher, N., 2002. Igneous zircon: trace element composition as an indicator of source rock type. Contrib. Mineral. Petrol. 143, 602–622.

Blevin, P.L., 2004. Redox and compositional parameters for interpreting the granitoid metallogeny of Eastern Australia: implications for gold-rich ore systems. Resour. Geol. 54, 241–252.

Bordage, A., Balan, E., de Villiers, J.P.R., Cromarty, R., Juhin, A., Carvallo, C., Calas, G., Raju, P.V.S., Glatzel, P., 2011. V oxidation state in Fe-Ti oxides by high-energy resolution fluorescence-detected X-ray absorption spectroscopy. Phys. Chem. Miner. 38, 449–458.

Buddington, A.F., Lindsley, D.H., 1964. Iron–titanium oxide minerals and synthetic equivalents. J. Petrol. 5, 310–357.

Burnham, A.D., Berry, A.J., 2014. The effect of oxygen fugacity, melt composition, temperature and pressure on the oxidation state of cerium in silicate melts. Chem. Geol. 366, 52–60.

Calmus, T., Aguillón-Robles, A., Maury, R.C., Bellon, H., Benoit, M., Cotton, J., Bourgois, J., Michaud, F., 2003. Spatial and temporal evolution of basalts and magnesian andesites ("bajaites") from Baja California, Mexico: the role of slab melts. Lithos 66, 77–105.

Castillo, P.R., 2012. Adakite petrogenesis. Lithos 134–135, 304–316.

Chen, L., Zheng, T., Xu, W., 2006. A thinned lithospheric image of the Tanlu Fault Zone, eastern China: constructed from wave equation based receiver function migration. J. Geophys. Res. 111, B09312.

Chen, B., Jahn, B.M., Suzuki, K., 2013. Petrological and Nd-Sr-Os isotopic constraints on the origin of high-Mg adakitic rocks from the North China Craton: tectonic implications. Geology 41, 91–94.

Chu, Z.Y., Wu, F.Y., Walker, R.J., Rudnick, R.L., Pitcher, L., Puchtel, I.S., Yang, Y.H., Wilde, S.A., 2009. Temporal evolution of the lithospheric mantle beneath the eastern North China Craton. J. Petrol. 50, 1857–1898.

Claiborne, L.L., Miller, C.F., Walker, B.A., Wooden, J.L., Mazdab, F.K., Bea, F., 2006. Tracking magmatic processes through Zr/Hf ratios in rocks and Hf and Ti zoning in zircons: an example from the Spirit Mountain batholith, Nevada. Mineral. Mag. 70, 517–543.

Claiborne, L.L., Miller, C.F., Wooden, J.L., 2010. Trace element composition of igneous zircon: a thermal and compositional record of the accumulation and evolution of a large silicic batholith, Spirit Mountain, Nevada. Contrib. Mineral. Petrol. 160, 511–531.

Cole, J.W., Thordarson, T., Burt, R.M., 2000. Magma origin and evolution of White Island (Whakaari) volcano, Bay of Plenty, New Zealand. J. Petrol. 41, 867–895.

Collerson, K.D., Kamber, B.S., Schoenberg, R., 2002. Applications of accurate, high-precision Pb isotope ratio measurement by multi-collector ICP-MS. Chem. Geol. 188, 65–83.

Defant, M.J., Drummond, M.S., 1990. Derivation of some modern arc magmas by melting of young subducted lithosphere. Nature 347, 662–665.

Deng, J., Yang, X., Qi, H., Zhang, Z.F., Mastoi, A.S., Sun, W., 2017. Early Cretaceous high-Mg adakites associated with Cu-Au mineralization in the Cebu Island, Central Philippines: implication for partial melting of the paleo-Pacific Plate. Ore Geol. Rev. 88, 251–269.

Duan, Z., Li, J.W., 2017. Zircon and titanite U-Pb dating of the Zhangjiawa iron skarn deposit, Luxi district, North China Craton: implications for a craton-wide iron skarn mineralization. Ore Geol. Rev. 89, 309–323.

Fan, W.M., Zhang, H.F., Baker, J., Jarvis, K.E., Mason, P.R.D., Menzies, M.A., 2000. On and off the North China Craton: where is the Archaean keel? J. Petrol. 41, 933–950.

Ferry, J.M., Watson, E.B., 2007. New thermodynamic models and revised calibrations for the Ti-in-zircon and Zr-in-rutile thermometers. Contrib. Mineral. Petrol. 154, 429–437.

Frost, B.F., 1991. Introduction to oxygen fugacity and its petrologic importance. Rev. Mineral. 25, 1–10.

Fu, B., Page, F.Z., Cavosie, A.J., Fournelle, J., Kita, N.T., Lackey, J.S., Wilde, S.A., Valley, J.W., 2008. Ti-in-zircon thermometry: applications and limitations. Contrib. Mineral. Petrol. 156, 197–215.

Gao, S., Luo, T.C., Zhang, B.R., Zhang, H.F., Han, Y.W., Zhao, Z.D., Hu, Y.K., 1998. Chemical composition of the continental crust as revealed by studies in East China. Geochim. Cosmochim. Acta 62, 1959–1975.

Gao, S., Rudnick, R., Carlson, R.W., McDonough, W.F., Liu, Y.S., 2002. Re-Os evidence for replacement of ancient mantle lithosphere beneath the North China Craton. Earth Planet. Sci. Lett. 198, 307–322.

Gao, S., Rudnick, R.L., Xu, W.L., Yuan, H.L., Liu, Y.S., Walker, R.J., Puchtel, I.S., Liu, X., Huang, H., Wang, X.R., Yang, J., 2008. Recycling deep cratonic lithosphere and generation of intraplate magmatism in the North China Craton. Earth Planet. Sci. Lett. 270, 41–53.

Guo, F., Fan, W.M., Wang, Y.J., Lin, G., 2001. Late Mesozoic mafic intrusive complexes in the North China Block: constrains on the nature of sub-continental lithospheric mantle. Phys. Chem. Earth A 26, 759–771.

Guo, F., Fan, W., Wang, Y., Lin, G., 2003. Geochemistry of late Mesozoic mafic magmatism in west Shandong Province, eastern China: characterizing the lost lithospheric mantle beneath the North China Block. Geochem. J. 37, 63–77.

Hanchar, J.M., van Westrenen, W., 2007. Rare earth element behavior in zircon-melt systems. Elements 3, 37–42.

Harrison, T.M., Watson, E.B., Aikman, A.B., 2007. Temperature spectra of zircon crystallization in plutonic rocks. Geology 35, 635–638.

Hawthorne, F.C., Oberti, R., Harlow, G.E., Maresch, W.V., Martin, R.F., Schumacher, J.C., Welch, M.D., 2012. Nomenclature of the amphibole supergroup. Am. Mineral. 97, 2031–2048.

Heaman, L.M., Bowins, R., Crocket, J., 1990. The chemical composition of igneous zircon suites: implications for geochemical tracer studies. Geochim. Cosmochim. Acta 54, 1597–1607.

Hildreth, W., Moorbath, S., 1988. Crustal contributions to arc magmatism in the Andes of central Chile. Contrib. Mineral. Petrol. 98, 455–489.

Holloway, J.R., 1976. Fluids in the evolution of granitic magmas: consequences of finite CO_2 solubility. Geol. Soc. Am. Bull. 87, 1513–1518.

Hou, T., Zhang, Z., Encarnacion, J., Du, Y., Zhao, Z., Liu, J., 2010. Geochemistry of Late Mesozoic dioritic porphyries associated with Kiruna-style and stratabound carbonate-hosted Zhonggu iron ores, Middle–Lower Yangtze Valley, Eastern China: constraints on petrogenesis and iron sources. Lithos 119, 330–344.

Hou, T., Zhang, Z., Encarnacion, J., Huang, H., Wang, M., 2012. Geochronology/geochemistry of the Washan dioritic porphyry associated with Kiruna-type iron ores, Middle-Lower Yangtze River Valley, eastern China: implications for petrogenesis/mineralization. Int. Geol. Rev. 54, 1332–1352.

Huang, X.L., Zhong, J.W., Xu, Y.G., 2012. Two tales of the continental lithospheric mantle prior to the destruction of the North China Craton: insights from Early Cretaceous mafic intrusions in western Shandong, East China. Geochim. Cosmochim. Acta 96, 193–214.

Jahn, B.M., Auvray, B., Shen, Q.H., Liu, D.Y., Zhang, Z.Q., Dong, Y.J., Ye, X.J., Zhang, Q.Z., Cornichet, J., Mace, J., 1988. Archean crustal evolution in China: the Taishan complex, and evidence for juvenile crustal addition from long-term depleted mantle. Precambrian Res. 38, 381–403.

Jahn, B.M., Wu, F., Lo, C.H., Tsai, C.H., 1999. Crust-mantle interaction induced by deep subduction of the continental crust: geochemical and Sr-Nd isotopic evidence from post-collisional mafic-ultramafic intrusions of the northern Dabie complex, central China. Chem. Geol. 157, 119–146.

Jin, Z., Zhang, Z., Hou, T., Santosh, M., Han, L., 2015. Genetic relationship of high-Mg dioritic pluton to iron mineralization: a case study from the Jinling skarn-type iron deposit in the North China Craton. J. Asian Earth Sci. 113, 957–979.

Karsli, O., Dokuz, A., Uysal, İ., Aydin, F., Kandemir, R., Wijbrans, J., 2010. Generation of the Early Cenozoic adakitic volcanism by partial melting of mafic lower crust, Eastern Turkey: implications for crustal thickening to delamination. Lithos 114, 109–120.

Kelemen, P.B., 1995. Genesis of high Mg# andesites and the continental crust. Contrib. Mineral. Petrol. 120, 1–19.

Kelemen, P.B., Hanghøj, K., Greene, A.R., 2003. One view of the geochemistry of subduction-related magmatic arcs, with an emphasis on primitive andesite and lower crust. In: Holland, H.D., Turekian, K.K. (Eds.), Treatise on Geochemistry. Elsevier, Amsterdam, pp. 593–659.

Komiya, T., Maruyama, S., 2007. A very hydrous mantle under the western Pacific region: implications for formation of marginal basins and style of Archean plate tectonics. Gondwana Res. 11, 132–147.

Kong, Q.Y., Zhang, T.Z., Yu, X.F., Xu, J.X., Pan, Y.L., Li, X.S., 2006. Deposits in Shandong Province. Shandong Science and Technology Press, Jinan (902 pp.).
König, S., Schuth, S., Münker, C., Qopoto, C., 2007. The role of slab melting in the petrogenesis of high-Mg andesites: evidence from Simbo Volcano, Solomon Islands. Contrib. Mineral. Petrol. 153, 85–103.
Lan, T.G., Fan, H.R., Santosh, M., Hu, F.F., Yang, K.F., Yang, Y.H., Liu, Y.S., 2012. Early Jurassic high-K calc-alkaline and shoshonitic rocks from the Tongshi intrusive complex, eastern North China Craton: implication for crust-mantle interaction and post-collisional magmatism. Lithos 140–141, 183–199.
Langmuir, C.H., Vocke, R.D., Hanson, G.N., 1978. A general mixing equation with applications to Icelandic basalts. Earth Planet. Sci. Lett. 37, 380–392.
Lattard, D., Sauerzapf, U., Käsemann, M., 2005. New calibration data for the Fe–Ti oxide thermo-oxybarometers from experiments in the Fe–Ti–O system at 1 bar, 1,000–1,300 °C and a large range of oxygen fugacities. Contrib. Mineral. Petrol. 149, 735–754.
Lázaro, C., García-Casco, A., 2008. Geochemical and Sr–Nd isotope signatures of pristine slab melts and their residues, Sierra del Convento mélange, eastern Cuba. Chem. Geol. 255, 120–133.
Li, S.R., Santosh, M., 2014. Metallogeny and craton destruction: records from the North China Craton. Ore Geol. Rev. 56, 376–414.
Li, S.G., Chen, Y., Cong, B.L., Zhang, Z., Zhang, R., Liou, D., Hart, S.R., Ge, N., 1993. Collision of the North China and Yangtze blocks and formation of coesite-bearing eclogites: timing and processes. Chem. Geol. 109, 70–89.
Li, Q.Z., Xie, Z., Chen, J.F., Gao, T.S., Yu, G., Qian, H., 2007. Pb-Sr-Nd isotopic characteristics of the gabbros from Jinan and Zouping and the contribution of the lower crust to the magma source. Geol. J. China Univ. 13, 297–310 (in Chinese with English abstract).
Li, Z.H., Qu, H.J., Gong, W.B., 2015. Late Mesozoic basin development and tectonic setting of the northern North China Craton. J. Asian Earth Sci. 114, 115–139.
Lin, S., Beakhouse, G.P., 2013. Synchronous vertical and horizontal tectonism at late stages of Archean cratonization and genesis of Hemlo gold deposit, Superior craton, Ontario, Canada. Geology 41, 359–362.
Liu, H., Wang, B., 1996. Geochemical characteristic of paleokarstification of Ordovician Majiagou carbonates in Xingxian and Liulin, Shanxi, China. Carbonates Evaporites 11, 77–84 (in Chinese with English abstract).
Liu, S., Xia, Q., 2014. Water content in the early Cretaceous lithospheric mantle beneath the south-central Taihang Mountains: implications for the destruction of the North China Craton. Chin. Sci. Bull. 59, 1362–1365.
Liu, Y.S., Gao, S., Yuan, H.L., Zhou, L., Liu, X.M., Wang, X.C., Hu, Z.C., Wang, L.S., 2004a. U-Pb zircon ages and Nd, Sr and Pb isotopes of lower crustal xenoliths from North China Craton: insights on evolution of lower continental crust. Chem. Geol. 211, 87–109.
Liu, J.M., Zhang, H.F., Sun, J.G., Ye, J., 2004b. Geochemical research on C-O and Sr-Nd isotopes of mantle-derived rocks from Shandong Province, China. Sci. China Ser. D Earth Sci. 47, 171–180.
Liu, Y.S., Hu, Z.C., Gao, S., Günther, D., Xu, J., Gao, C.G., Chen, H.H., 2008. In situ analysis of major and trace elements of anhydrous minerals by LA-ICP-MS without applying an internal standard. Chem. Geol. 257, 34–43.
Liu, Y.S., Hu, Z.C., Zong, K.Q., Gao, C.G., Gao, S., Xu, J., Chen, H.H., 2010a. Reappraisement and refinement of zircon U-Pb isotope and trace element analyses by LA-ICP-MS. Chin. Sci. Bull. 55, 1535–1546.
Liu, S.A., Li, S.G., He, Y.S., Huang, F., 2010b. Geochemical contrasts between early Cretaceous ore-bearing and ore-barren high-Mg adakites in central-eastern China: implications for petrogenesis and Cu–Au mineralization. Geochim. Cosmochim. Acta 74, 7160–7178.
Liu, X., Zhao, D., Li, S., Wei, W., 2017. Age of the subducting Pacific slab beneath East Asia and its geodynamic implications. Earth Planet. Sci. Lett. 464, 166–174.
Liu, Q.Q., Chi, Q.H., Wang, X.Q., Zhou, J., Liu, H.L., Liu, D.S., Gao, Y.F., Zhai, D.X., 2018. Distribution and influencing factors of rare earth elements in carbonate rocks along three continental-scale transects in eastern China. Earth Sci. Front. 25, 99–115 (in Chinese with English abstract).
Locock, A.J., 2014. An Excel spreadsheet to classify chemical analyses of amphiboles following the IMA 2012 recommendations. Comput. Geosci. 62, 1–11.
Lu, S., Zhao, G., Wang, H., Hao, G., 2008. Precambrian metamorphic basement and sedimentary cover of the North China Craton: a review. Precambrian Res. 160, 77–93.
Ludwig, K.R., 2003. User's Manual for Isoplot 300: A Geochronolgical Toolkit for Microsoft Excel. 4. Berkeley Geochronological Center Special Publication, pp. 25–32.
Lugmair, G.W., Harti, K., 1978. Lunar initial $^{143}Nd/^{144}Nd$: differential evolution of the lunar crust and mantle. Earth Planet. Sci. Lett. 39, 349–357.
Ma, J.Q., Xu, X.L., Yuan, P.M., 2004. Discussion on mineralization rule of Jinling diggings. Shandong Metall. 26, 6–8 (in Chinese with English abstract).
Manya, S., Maboko, M.A.H., Nakamura, E., 2007. The geochemistry of high-Mg andesite and associated adakitic rocks in the Musoma-Mara Greenstone Belt, northern Tanzania: possible evidence for Neoarchaean ridge subduction? Precambrian Res. 159, 241–259.
Mao, J.W., Pirajno, F., Cook, N.J., 2011. Mesozoic metallogeny in East-China and corresponding geodynamic settings-an introduction to the special issue. Ore Geol. Rev. 43, 1–7.
Mao, J.W., Duan, C., Liu, J.L., Zhang, C., 2012. Metallogeny and corresponding mineral deposit model of the Cretaceous terrestrial volcanic-intrusive rocks-related polymetallic iron deposits in Middle-Lower Yangtze River Valley. Acta Petrol. Sin. 28, 1–14 (in Chinese with English abstract).
Martin, H., Smithies, R.H., Rapp, R., Moyen, J.F., Champion, D., 2005. An overview of adakite, tonalite-trondhjemite-granodiorite, TTG, and sanukitoid: relationships and some implications for crustal evolution. Lithos 79, 1–24.
Maruyama, S., Okamoto, K., 2007. Water transportation from the subducting slab into the mantle transition zone. Gondwana Res. 11, 148–165.
Maruyama, S., Isozaki, Y., Kimura, G., Terabayashi, M., 1997. Paleogeographic maps of the Japanese Islands: plate tectonic synthesis from 750 Ma to the present. Island Arc 6, 121–142.
Meinert, L.D., 1995. Compositional variation of igneous rocks associated with skarn deposits-chemical evidence for a genetic connection between petrogenesis and mineralization. In: Thompson, J.F.H. (Ed.), Magmas, Fluids and Ore Deposits. Mineralogical Association of Canada Short Course. vol. 23, pp. 401–418.
Meinert, L.D., Dipple, G.M., Nicolescu, S., 2005. World skarn deposits. Econ. Geol. 299–336 100th Anniversary Volume.
Meng, Q.R., Zhang, G.W., 1999. Timing of collision of the North and South China blocks: controversy and reconciliation. Geology 27, 123–126.
Middlemost, E.A.K., 1994. Naming materials in the magma/igneous rock system. Earth-Sci. Rev. 37, 215–224.
Mueller, A., 2007. Copper-gold endoskarns and high-Mg monzodiorite–tonalite intrusions at Mt Shea, Kalgoorlie, Australia: implications for the origin of gold-pyrite-tennantite mineralization in the Golden Mile. Mineral. Deposita 42, 737–769.
Mungall, J.E., 2002. Roasting the mantle: slab melting and the genesis of major Au and Au-rich Cu deposits. Geology 30, 915–918.
Nadoll, P., Koenig, A.E., 2011. LA-ICP-MS of magnetite: methods and reference materials. J. Anal. At. Spectrom. 26, 1872–1877.
Pirajno, F., Zhou, T., 2015. Intra-continental porphyry and porphyry-skarn mineral systems in Eastern China: scrutiny of a special case “made-in-China”. Econ. Geol. 110, 603–629.
Pirajno, F., Ernst, R.E., Borisenko, A.S., Fedoseev, G., Naumov, E.A., 2009. Intraplate magmatism in Central Asia and China and associated metallogeny. Ore Geol. Rev. 35, 114–136.
Polat, A., Li, J., Fryer, B., Kusky, T., Gagnon, J., Zhang, S., 2006. Geochemical characteristics of the Neoarchean., 2800–2700 Ma. Taishan greenstone belt, North China Craton: evidence for plume-craton interaction. Chem. Geol. 230, 60–87.
Qian, Q., Hermann, J., 2010. Formation of high-Mg diorites through assimilation of peridotite by monzodiorite magma at crustal depths. J. Petrol. 51, 1381–1416.
Qiu, J., Lo, C.H., McInnes, B.I.A., Zhou, J., 2000. Potash-rich magmatism and associated gold-copper mineralization in the Yishu deep fault zone and its vicinity, eastern China. Resour. Geol. 50, 269–280.
Rapp, R.P., Shimizu, N., Norman, M.D., Applegate, G.S., 1999. Reaction between slab-derived melts and peridotite in the mantle wedge: experimental constraints at 38 GPa. Chem. Geol. 160, 335–356.
Ren, J., Tamaki, K., Li, S., Zhang, J., 2002. Late Mesozoic and Cenozoic rifting and its dynamic setting in eastern China and adjacent areas. Tectonophysics 344, 175–205.
Richards, J.P., 2003. Tectono-magmatic precursors for porphyry Cu-(Mo-Au) deposit formation. Econ. Geol. 98, 1515–1533.
Richards, J.P., 2011. Magmatic to hydrothermal metal fluxes in convergent and collided margins. Ore Geol. Rev. 40, 1–26.
Richards, J.P., 2013. Giant ore deposits formed by optimal alignments and combinations of geological processes. Nat. Geosci. 6, 911–916.
Ridolfi, F., Renzulli, A., Puerini, M., 2010. Stability and chemical equilibrium of amphibole in calc-alkaline magmas: an overview, new thermobarometric formulations and application to subduction-related volcanoes. Contrib. Mineral. Petrol. 160, 45–66.
Rudnick, R.L., 1995. Making continental crust. Nature 378, 571–578.
Sajona, F.G., Maury, R.C., Pubellier, M., Leterrier, J., Bellon, H., Cotton, J., 2000. Magmatic source enrichment by slab-derived melts in a young post-collision setting, central Mindanao (Philippines). Lithos 54, 173–206.
Simon, A.C., Pettke, T., Candela, P.A., Piccoli, P.M., Heinrich, C.A., 2004. Magnetite solubility and iron transport in magmatic-hydrothermal environments. Geochim. Cosmochim. Acta 68, 4905–4914.
Smythe, D.J., Brenan, J.M., 2016. Magmatic oxygen fugacity estimated using zircon-melt partitioning of cerium. Earth Planet. Sci. Lett. 453, 260–266.
Spencer, K.J., Lindsley, D.H., 1981. A solution model for coexisting iron-titanium oxides. Am. Mineral. 66, 1189–1201.
Sun, S.S., McDonough, W.F., 1989. Chemical and isotopic systematics of oceanic basalts: implications for mantle composition and processes. In: Saunders, A.D., Norry, M.J. (Eds.), Magmatism in the Oceanic Basalts. 42. Geological Society, London, pp. 313–345 Special Publications.
Sun, W.D., Ding, X., Hu, Y.H., Li, X.H., 2007. The golden transformation of the Cretaceous plate subduction in the west Pacific. Earth Planet. Sci. Lett. 262, 533–542.
Sun, Y., Xiao, L., Zhan, Q., Wu, J., Zhu, D., Huang, W., Bai, M., Zhang, Y., 2015. Petrogenesis of the Kuangshancun and Hongshan intrusive complexes from the Handan–Xingtai district: implications for iron mineralization associated with Mesozoic magmatism in the North China Craton. J. Asian Earth Sci. 113, 1162–1178.
Takagi, T., Tsukimura, K., 1997. Genesis of oxidized- and reduced-type granites. Econ. Geol. 92, 81–86.
Tang, Y.J., Zhang, H.F., Santosh, M., Ying, J.F., 2013. Differential destruction of the North China Craton: a tectonic perspective. J. Asian Earth Sci. 78, 71–82.
Tatsumi, Y., 2001. Geochemical modeling of partial melting of subducting sediments and subsequent melt-mantle interaction: generation of high-Mg andesites in the Setouchi volcanic belt, southwest Japan. Geology 29, 323–326.
Tatsumi, Y., 2008. Making continental crust: the sanukitoid connection. Chin. Sci. Bull. 53, 1620–1633.
Toplis, M.J., Carroll, M.R., 1995. An experimental study of the influence of oxygen fugacity on Fe-Ti oxide stability, phase relations, and mineral-melt equilibria in ferro-basaltic systems. J. Petrol. 36, 1137–1170.
Toplis, M.J., Corgne, A., 2002. An experimental study of element partitioning between magnetite, clinopyroxene and iron-bearing silicate liquids with particular emphasis on vanadium. Contrib. Mineral. Petrol. 144, 22–37.
Trail, D., Watson, E.B., Tailby, N.D., 2012. Ce and Eu anomalies in zircon as proxies for oxidation state of magmas. Geochim. Cosmochim. Acta 97, 70–87.

Valley, J.W., Cavosie, A.J., Fu, B., Peck, W.H., Wilde, S.A., 2006. Comment on "Heterogeneous Hadean Hafnium: evidence of continental crust at 44 to 45 Ga". Science 312 (1139a).
Wang, Y.J., Fan, W.M., Zhang, H.F., Peng, T.P., 2006. Early Cretaceous gabbroic rocks from the Taihang Mountains: implications for a paleosubduction-related lithospheric mantle beneath the central North China Craton. Lithos 86, 281–302.
Wang, Y., Zhang, Y., Zhao, G., Fan, W., Xia, X., Zhang, F., Zhang, A., 2009. Zircon U-Pb geochronological and geochemical constraints on the petrogenesis of the Taishan sanukitoids, Shandong: implications for Neoarchean subduction in the Eastern Block, North China Craton. Precambrian Res. 174, 273–286.
Wang, Q., Li, Z.X., Chung, S.L., Wyman, D.A., Sun, Y.L., Zhao, Z.H., Zhu, Y.T., Qiu, H.N., 2011. Late Triassic high-Mg andesite/dacite suites from northern Hohxil, North Tibet: geochronology, geochemical characteristics, petrogenetic processes and tectonic implications. Lithos 126, 54–67.
Watson, E.B., Harrison, T.M., 2005. Zircon thermometer reveals minimum melting conditions on earliest earth. Sciences 308, 841–844.
Watson, E.B., Wark, D.A., Thomas, J.B., 2006. Crystallization thermometers for zircon and rutile. Contrib. Mineral. Petrol. 151, 413–433.
Webster, J.D., 2004. The exsolution of magmatic hydrosaline chloride liquids. Chem. Geol. 210, 33–48.
Wei, J., Lv, D., Chen, X., 2011. Characteristics and distribution of condensed seam in continental sea coal-bearing sedimentation in Western Shandong. J. Shandong Univ. Sci. Technol. 30, 30–35 (in Chinese with English abstract).
Wei, X., Xu, Y.G., Feng, Y.X., Zhao, J.X., 2014. Plume-lithosphere interaction in the generation of the Tarim large igneous province, NW China: geochronological and geochemical constraints. Am. J. Sci. 314, 314–356.
Wen, G., Bi, S.J., Li, J.W., 2017. Role of evaporitic sulfates in iron skarn mineralization: a fluid inclusion and sulfur isotope study from the Xishimen deposit, Handan-Xingtai district, North China Craton. Mineral. Deposita 52, 495–514.
Whitney, J., Hemley, J., Simon, F., 1985. The concentration of iron in chloride solutions equilibrated with synthetic granitic compositions: the sulfur-free system. Econ. Geol. 80, 444–460.
Wilkinson, J.J., 2013. Triggers for the formation of porphyry ore deposits in magmatic arcs. Nat. Geosci. 6, 917–925.
Windley, B.F., Maruyama, S., Xiao, W.J., 2010. Delamination/thinning of sub-continental lithospheric mantle under Eastern China: the role of water and multiple subduction. Am. J. Sci. 310, 1250–1293.
Wright, J.B., 1969. A simple alkalinity ratio and its application to questions of non-orogenic granite genesis. Geol. Mag. 106, 370–384.
Wu, F.Y., Lin, J.Q., Wilde, S.A., Zhang, X.O., Yang, J.H., 2005. Nature and significance of the Early Cretaceous giant igneous event in eastern China. Earth Planet. Sci. Lett. 233, 103–119.
Xia, Q.K., Liu, J., Liu, S.C., Kovácsb, I., Feng, M., Dang, L., 2013. High water content in the Mesozoic lithospheric mantle of the North China Craton and implications for its destruction. Earth Planet. Sci. Lett. 361, 85–97.
Xiao, W., Windley, B.F., Hao, J., Zhai, M., 2003. Accretion leading to collision and the Permian Solonker suture, Inner Mongolia, China: termination of the Central Asian Orogenic belt. Tectonics 22 (8-1–8-20).
Xu, Y.G., 2014. Recycled oceanic crust in the source of 90–40 Ma basalts in North and Northeast China: evidence, provenance and significance. Geochim. Cosmochim. Acta 143, 49–67.
Xu, Y.G., Huang, X.L., Ma, J.L., Wang, Y.B., Iizuka, Y., Xu, J.F., Wang, Q., Wu, X.Y., 2004a. Crust-mantle interaction during the tectono-thermal reactivation of the North China Craton: constraints from SHRIMP zircon U–Pb chronology and geochemistry of Mesozoic plutons from western Shandong. Contrib. Mineral. Petrol. 147, 750–767.
Xu, Y.G., Ma, J.L., Huang, X.L., Iizuka, Y., Chung, S.L., Wang, Y.B., Wu, X.Y., 2004b. Early Cretaceous gabbroic complex from Yinan, Shandong Province: petrogenesis and mantle domains beneath the North China Craton. Int. J. Earth Sci. 93, 1025–1041.
Xu, W., Hergt, J.M., Gao, S., Pei, F., Wang, W., Yang, D., 2008. Interaction of adakitic melt-peridotite: implications for the high-Mg# signature of Mesozoic adakitic rocks in the eastern North China Craton. Earth Planet. Sci. Lett. 265, 123–137.
Xu, W.W., Zheng, T.Y., Zhao, L., 2011. Mantle dynamics of the reactivating North China Craton: constraints from the topographies of the 410-km and 660-km discontinuities. Sci. China Earth Sci. 54, 881–887.
Xu, W.L., Zhou, Q.J., Pei, F.P., Yang, D.B., Gao, S., Li, Q.L., Yang, Y.H., 2013. Destruction of the North China Craton: delamination or thermal/chemical erosion? Mineral chemistry and oxygen isotope insights from websterite xenoliths. Gondwana Res. 23, 119–129.
Yang, Y.H., Wu, F.Y., Wilde, S.A., Liu, X.M., Zhang, Y.B., Xie, L.W., Yang, J.H., 2009. In situ perovskite Sr-Nd isotopic constraints on the petrogenesis of the Ordovician Mengyin kimberlites in the North China Craton. Chem. Geol. 264, 24–42.
Yang, D.B., Xu, W.L., Pei, F.P., Yang, C.H., Wang, Q.H., 2012a. Spatial extent of the influence of the deeply subducted South China Block on the southeastern North China Block: constraints from Sr-Nd-Pb isotopes in Mesozoic mafic igneous rocks. Lithos 136–139, 246–260.
Yang, Q.L., Zhao, Z.F., Zheng, Y.F., 2012b. Modification of subcontinental lithospheric mantle above continental subduction zone: constraints from geochemistry of Mesozoic gabbroic rocks in southeastern North China. Lithos 146–147, 164–182.
Yang, Z.M., Lu, Y.J., Hou, Z.Q., Chang, Z.S., 2015. High-Mg diorite from Qulong in southern Tibet: implications for the genesis of adakite-like intrusions and associated porphyry Cu deposits in collisional orogens. J. Petrol. 56, 227–254.
Yang, D.B., Yang, H.T., Shi, J.P., Xu, W.L., Wang, F., 2017. Sedimentary response to the paleogeographic and tectonic evolution of the southern North China Craton during the late Paleozoic and Mesozoic. Gondwana Res. 49, 278–295.
Ying, J.F., Zhang, H.F., Tang, Y.J., 2010. Lower crustal xenoliths from Junan, Shandong province and their bearing on the nature of the lower crust beneath the North China Craton. Lithos 119, 363–376.
Yogodzinski, G.M., Kay, R.W., Volynets, O.N., Koloskov, A.V., Kay, S.M., 1995. Magnesian andesite in the western Aleutian Komandorsky region: implications for slab melting and processes in the mantle wedge. Geol. Soc. Am. Bull. 107, 505–519.
Zhai, M.G., Santosh, M., 2011. The early Precambrian odyssey of the North China Craton: a synoptic overview. Gondwana Res. 20, 6–25.
Zhang, H.F., Sun, M., Zhou, X.H., Fan, W.M., Zhai, M.G., Ying, J.F., 2002. Mesozoic lithosphere destruction beneath the North China Craton: evidence from major-, trace-element and Sr-Nd-Pb isotope studies of Fangcheng basalts. Contrib. Mineral. Petrol. 144, 241–253.
Zhang, H.F., Sun, M., Zhou, X.H., Ying, J.F., 2005. Geochemical constraints on the origin of Mesozoic alkaline intrusive complexes from the North China Craton and tectonic implications. Lithos 81, 297–317.
Zhang, X.M., Zhang, Y.Q., Ji, W., 2007. Fault distribution patterns of the Luxi Block, Shandong, and Mesozoic sedimentary-magmatic-structural evolution sequence. J. Geom. 13, 163–172 (in Chinese with English abstract).
Zhang, Y.M., Gu, X.X., Liu, L., Dong, S.Y., Li, K., Li, B.H., Lv, P.R., 2011. Fluid inclusion and H-O isotope evidence for immiscibility during mineralization of the Yinan Au–Cu–Fe deposit, Shandong, China. J. Asian Earth Sci. 42, 83–96.
Zhang, Z., Hou, T., Santosh, M., Li, H., Li, J., Zhang, Z., Song, X., Wang, M., 2014. Spatio-temporal distribution and tectonic settings of the major iron deposits in China: an overview. Ore Geol. Rev. 57, 247–263.
Zhang, J.Q., Li, S.R., Santosh, M., Wang, J.Z., Li, Q., 2015. Mineral chemistry of high-Mg diorites and skarn in the Han-Xing Iron deposits of South Taihang Mountains, China: constraints on mineralization process. Ore Geol. Rev. 64, 200–214.
Zhao, G., Cawood, P.A., Li, S., Wilde, S.A., Sun, M., Zhang, J., He, Y., Yin, C., 2012. Amalgamation of the North China Craton: key issues and discussion. Precambrian Res. 222–223, 55–76.
Zhao, D., Isozaki, Y., Maruyama, S., 2017. Seismic imaging of the Asian orogens and subduction zones. J. Asian Earth Sci. 145, 349–367.
Zheng, J.P., Lu, F.X., 1999. Mantle xenoliths from kimberlites, Shandong and Liaoning: Paleozoic mantle character and its heterogeneity. Acta Petrol. Sin. 15, 65–74 (in Chinese with English abstracts).
Zheng, J.P., O'Reilly, S.Y., Griffin, W.L., Lu, F.X., Zhang, M., Pearson, N.J., 2001. Relics of refractory mantle beneath the eastern North China block: significance for lithosphere evolution. Lithos 57, 43–66.
Zhou, X.M., Li, W.X., 2000. Origin of Late Mesozoic igneous rocks in Southeastern China: implications for lithosphere subduction and underplating of mafic magmas. Tectonophysics 326, 269–287.
Zhu, R.X., Xu, Y.G., Zhu, G., Zhang, H.F., Xia, Q.K., Zheng, T.Y., 2012. Destruction of the North China Craton. Sci. China Earth Sci. 55, 1565–1587.
Zindler, A., Hart, S.R., 1986. Chemical geodynamics. Annu. Rev. Earth Planet. Sci. 14, 493–571.
Zong, X.D., Xu, J., Lu, T.Y., Fang, C.C., 2010. Stuctural types, ore body styles and occurrence pattern of large, large-medium iron deposits in Kuangshan iron ore field, Shandong Province. Contrib. Geol. Miner. Resour. Res. 25, 234–240 (in Chinese with English abstract).
Zong, X.D., Li, W., Zhao, H.S., Fan, C.C., Peng, C., 2011. The contact metasomatic-hydrothermal iron deposit in Laiwu, Shandong Province: multi-factor metallogenesis. Geol. Resour. 20, 370–375 (in Chinese with English abstract).
Zong, X.D., Li, W., Wang, J., Qiao, W., Zhang, J.F., Liu, J.T., 2012. Study on rich iron ore for martin steel and the by-products of Cu and Co in Zhangjiawa iron deposit of Shandong Province. Contrib. Geol. Miner. Resour. Res. 27, 60–65 (in Chinese with English abstract).
Zou, H.B., Zindler, A., Xu, X.S., Qi, Q., 2000. Major, trace element, and Nd, Sr and Pb isotope studies of Cenozoic basalts in SE China: mantle sources, regional variations, and tectonic significance. Chem. Geol. 171, 33–47.